Electronic Supporting Information

In situ X-ray diffraction investigation of NiS_x-formation on Ni-foam using chemical vapor deposition with H_2S

Soffi Ester Sola Olesen,[a,b] Magnus Kløve,[a] Anders Bæk Borup,[a] Andreas Dueholm Bertelsen,[a] Marcus Viktor Kragh-Schwarz,[b,c] Thorbjørn Erik Køppen Christensen,[d,e] Frederik Holm Gjørup,[a,d] Mads Ry Vogel Jørgensen,[a,d] Jacopo Catalano,*[c] Anders W. Jensen,[b] and Bo B. Iversen*[a]

[a]Center for integrated Materials Research, Department of Chemistry and iNANO, Aarhus University, Langelandsgade 140, 8000 Aarhus, Denmark.

[b]HydrogenPro ApS, Axel Gruhns Vej 3, 8270 Højbjerg, Denmark

[c]Department of Biological & Chemical Engineering, Aarhus University, Aabogade 40, 8200 Aarhus N, Denmark

[d]MAX IV Laboratory, Lund University, Fotongatan 2, 224 84 Lund, Sweden.

[e]Department of Applied Mathematics and Computer Science, Technical University of Denmark, Richard Petersens Plads 324, 2800 Kongens Lyngby, Denmark.

*Corresponding authors: jcatalano@au.dk, bo@chem.au.dk

Contents

1. Overview of samples and experiment

The following section includes the overview of sample and the experiments in Table S1, safety aspects in section 1.1, a schematic illustration of the synthesis setup in Figure S1, the approximation of the uniformity of the sample with the scale of Ni Figure S2, the SEM images of sample 130 °C, 0.5 mL/min in Figure S3. Furthermore, SEM and EDX in Figure S4 of sample 130 °C, 0.5 mL/min is provided as well as SEM and EDX over an induced crack in the coating for sample 130 °C, 5 mL/min in Figure S5.

Temp / flow of H_2S	70 °C	90 °C	110 °C	130 °C	150 °C	170 °C
0.1 mL/min	-	-	-	1	-	-
0.5 mL/min	1	1	1	3	1	1
1 mL/min	-	1	1	1	1	1
5 mL/min	-	-	-	1	-	-

Table S1 Overview of samples synthesized at different temperatures and flowrates. The numbers indicate the number of repetitions.

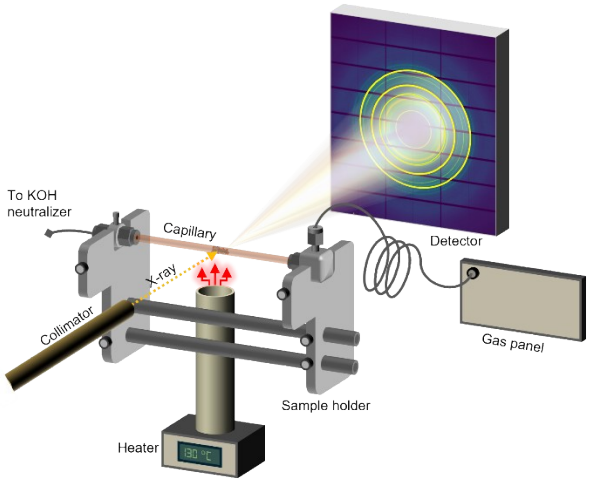

Figure S1 Schematic illustration of synthesis setup with X-rays in transmission geometry. Figure adapted from PhD dissertation of Rasmus Baden Stubkjær reproduced with permission.[1]

1.1 Description of safety aspects in the experiment

Leak Detection

The system was tested for leaks under argon gas flow at 5 mL/min using an LD-239 leak detector (GL Sciences) and leak detection spray to ensure airtightness.

H_2S Detection and Alarms

A handheld H_2S detector (GasAlertMicro 5 H_2S-CL2) was placed in the experimental hutch. This device triggers an alarm if H_2S levels reach 5 ppm, the Danish occupational exposure limit for H_2S. This model is widely used in the gas and oil industry for H_2S safety.

Two stationary H_2S detectors were installed: one in the gas-cylinder cabinet and one in the splash box. Both detectors are linked to a shut-off valve located downstream of the reduction valve. The shut-off valve is activated when H_2S concentrations exceed 5 ppm.

Fail-Safe Mechanisms

The three-way pneumatic valve features a spring-back function, ensuring automatic redirection to argon gas in the event of compressed air failure.

The mass flow controller closes automatically when power is off, to further prevent accidental H_2S release.

Neutralization System

A neutralizer system uses 30 wt% potassium hydroxide (KOH) to neutralize H_2S gas. pH indicators (phenolphthalein) confirm that the pH remains above 9, ensuring complete neutralization of H_2S.

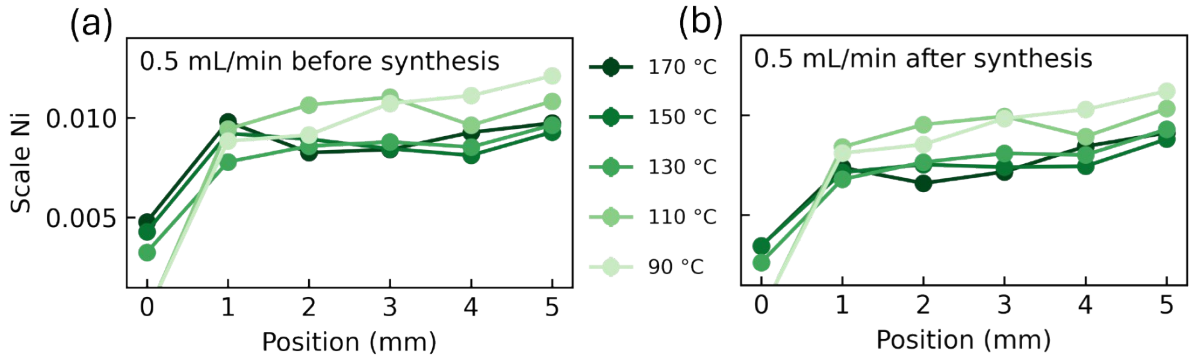

Figure S2 Uniformity of Ni foam samples depicted by the scale factor of Ni from Rietveld refinement for samples at all temperatures using a flow of 0.5 mL/min. (a) Before synthesis and (b) after synthesis

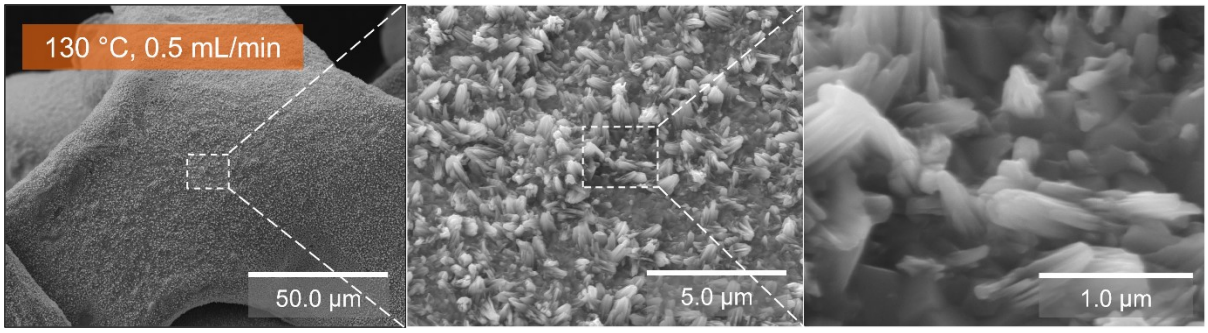

Figure S3 SEM of sample 130 °C, 0.5 mL/min at position 1.

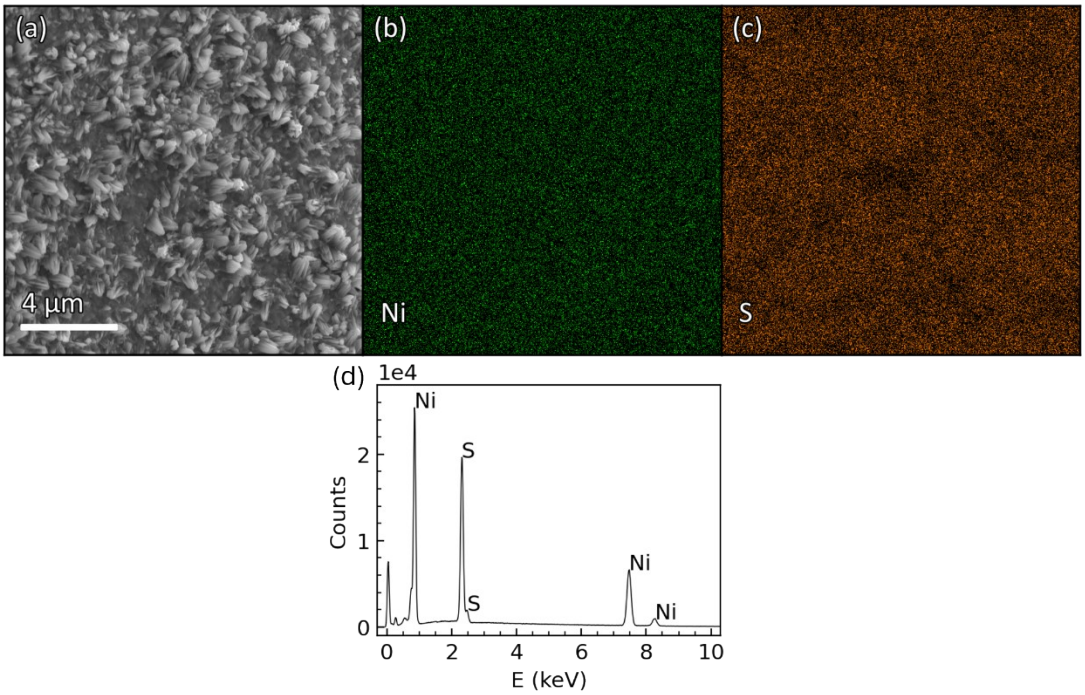

Figure S4 (a) SEM image of the inlet of H_2S (position 1) of the 130 °C, 0.5 mL/min sample with corresponding EDX maps of (b) Ni and (c) S. (d) EDX spectra corresponding to the elemental mapping.

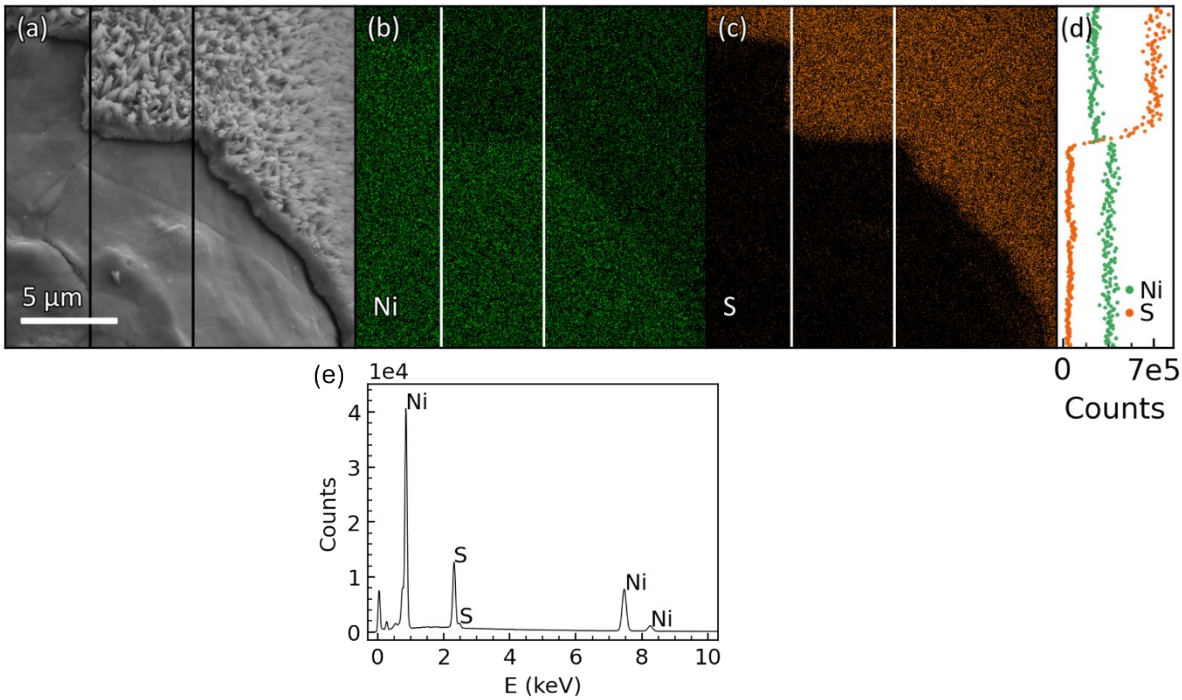

Figure S5 Sample treated at 5 mL/min H_2S at 130 °C. (a) SEM image of the inlet of H_2S (position 1) of the width corresponding EDX maps of (b) Ni and (c) S. The data were integrated along the x-axis in the highlighted region. The resulting profile was subsequently binned over 8 pixels in the y-direction to obtain

panel (d). The displayed counts correspond to the raw uncorrected counts. (e) EDX spectra corresponding to the elemental mapping.

2. Temperature series at position 1

The following section includes data collected and refined for the temperature series for flow of 0.5 mL/min, the kinetics of these. For the temperature series the raw PXRD pattern is found in Figure S6, the diffractogram on linear scale for sample 130 °C position 1 after 60 min in Figure S7, and the refined parameters in the Rietveld refinements shown in Figure S8. The Rietveld refinement was made with only refinement of crystallite size as the source of sample peak broadening; however, strain broadening could be applied as well. Due to the weak NiS_x peaks it was not possible to refine size and strain broadening simultaneously. Figure S6(a) shows that the peak broadening increases with both reaction temperature and time at temperatures above 110 °C, while remaining almost constant over time for samples 110 °C and 90 °C within the peak broadening resolution. For these experiments, the peak broadening could not be reliably determined until after ~15 min, most likely due to low phase contribution to the XRD pattern.

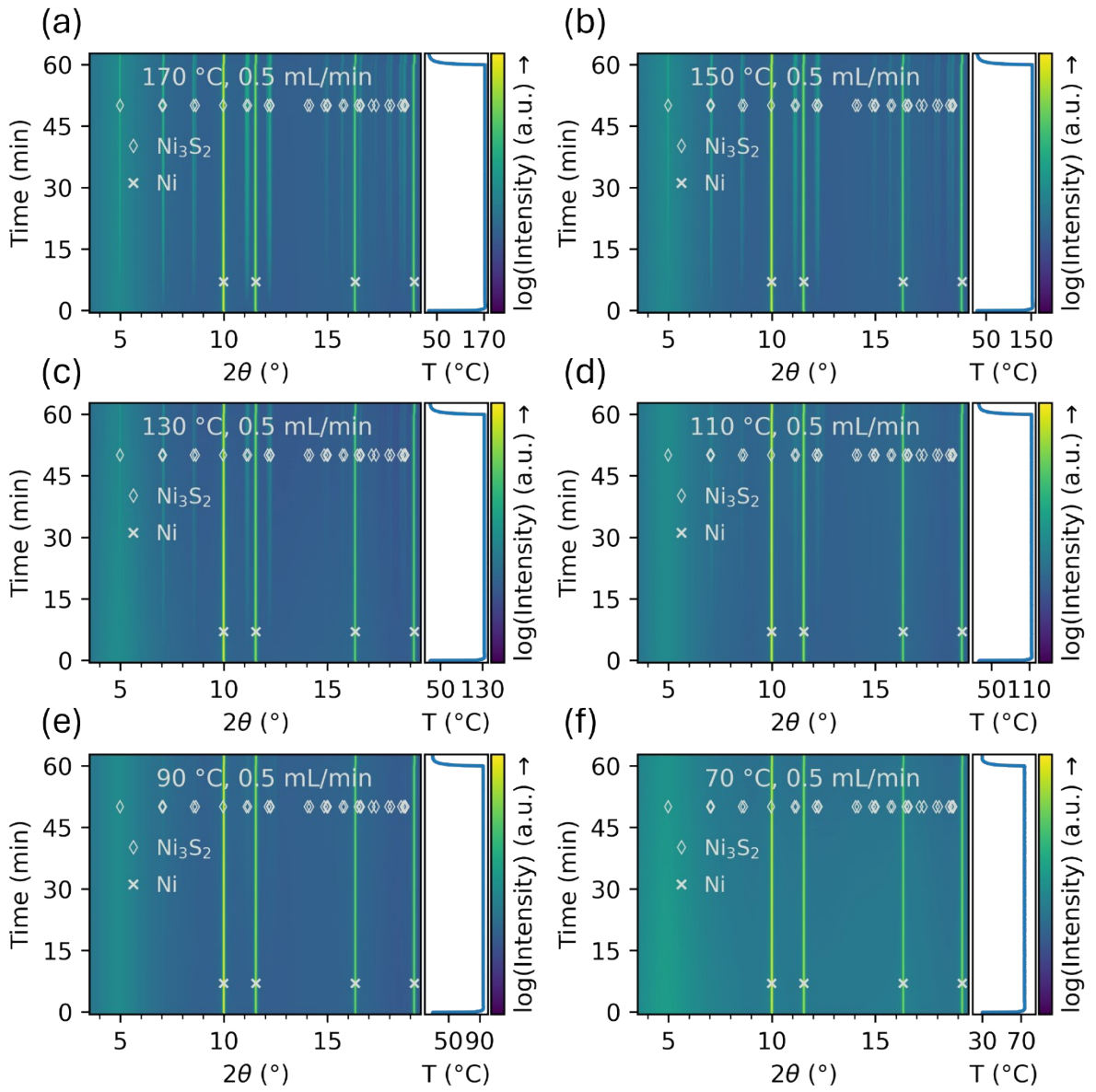

Figure S6 PXRD patterns as a function of time for samples 0.5 mL/min at (a) 170 °C, (b) 150 °C, (c) 130 °C, (d) 110 °C, (e) 90 °C, and (f) 70 °C. The PXRD patterns shown are collected at position 1.

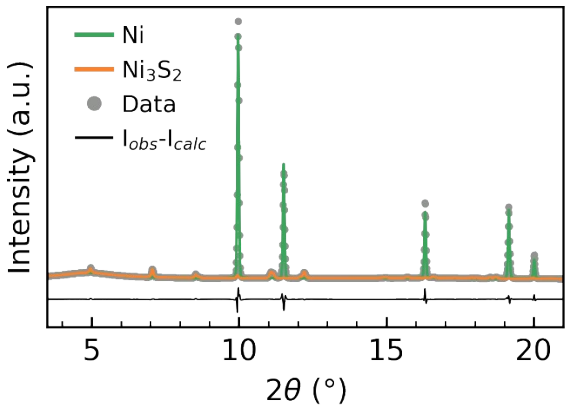

Figure S7 Refined PXRD pattern 60 min after the synthesis is initiated by heating for sample 130 °C, 0.5 mL/min at position 1. This diffractogram is shown on a linear scale, unlike the logarithmic scale used in Figure 2(b) of the main text.

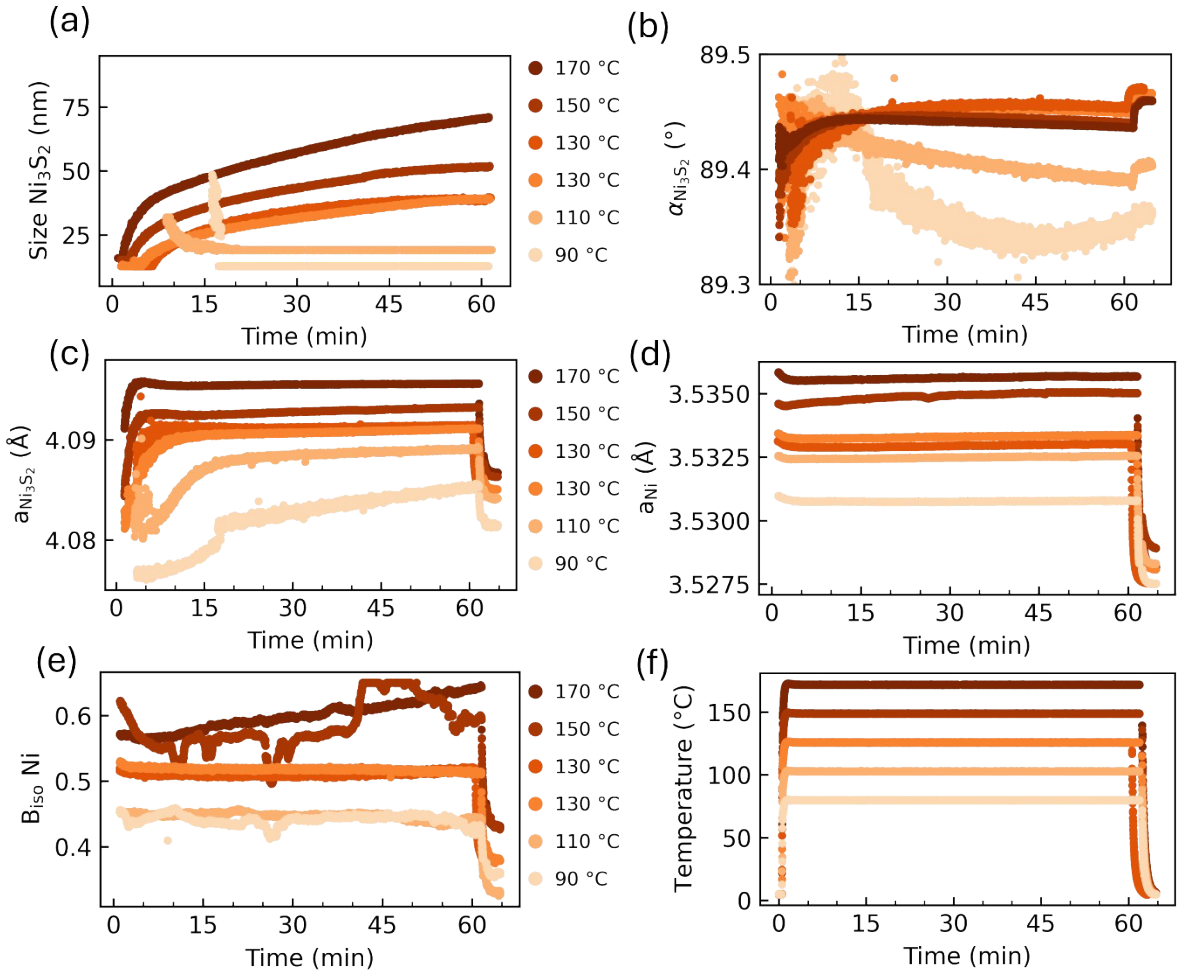

Figure S8 Obtained values from sequential Rietveld refinements for samples at flowrate 0.5 mL/min and temperatures 70-170 °C. The Rietveld refinements are performed on data collected at position 1. (a) Crystallite sizes of Ni_3S_2, however this could also be refined as strain (b) α of Ni_3S_2, (c) Unit cell parameter of Ni_3S_2, (d) unit cell parameter of Ni, (e) Isotropic B-values for Ni, and (f) the development in temperature during the experiments.

3. Model for H_2S reaction with Ni

The following section includes description of model of H_2S reaction with Ni, the model and assumptions, the fitting and the obtained results.

Assumptions and model

The formation of the thin Ni_3S_2 layer on the Ni substrate has been modelled by considering that H_2S diffuses through the layer of Ni_3S_2 formed and then it reacts with a fresh layer of Ni at the Ni- Ni_3S_2 interface. The physical system is represented in rectilinear coordinate system (see Figure S9), where the coordinate x is along the length of the capillary and the foam is placed at $x \in [0,5]mm$.

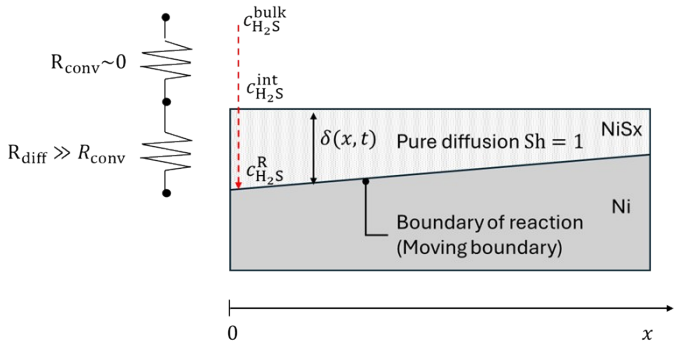

Figure S9 Schematic of the mass transfer model for Ni_3S_2 layer growth.

The assumptions of the model follow:

- H_2S penetrates the layer of Ni_3S_2 formed by pure diffusion. In dimensionless form this means:

$$Sh = h_m \cdot \frac{\delta(x,t)}{D_{H_2S-NiSx}} = 1$$

  Where Sh is the Sherwood number ($Sh = 1$ for pure diffusion), h_m is the mass transfer coefficient, $\delta(x,t)$ is the thickness of the Ni_3S_2 layer dependent on time t and the position x inside the capillary, and $D_{H_2S-NiSx}$ is the diffusion coefficient of H_2S in the Ni_3S_2 layer. Therefore, the H_2S flux, N''_{H_2S}, can be expressed as:

$$N''_{H_2S}(x,t) = h_m \cdot \left(c^{int}_{H_2S}(x,t) - c^{R}_{H_2S}(x,t)\right) = \frac{D_{H_2S-NiSx}}{\delta(x,t)} \cdot \left(c^{int}_{H_2S}(x,t) - c^{R}_{H_2S}(x,t)\right)$$

  where $c^{int}_{H_2S}$ and $c^{R}_{H_2S}$ are the H_2S concentrations at the Ni-gas and Ni- Ni_3S_2 interfaces, respectively.

- The bulk of the gas phase is considered well mixed ($R_{conv} = 0$):

$$c^{bulk}_{H_2S}(x,t) = c^{int}_{H_2S}(x,t) = c_{H_2S}(x,t)$$

  where $c^{bulk}_{H_2S}$ is the concentration of H_2S in the bulk of the gas phase. This assumption is reasonable since even for stagnant films (so even for no-flow condition) the diffusion coefficient of the reactant in the gas phase is more than 5 orders of magnitude larger than in the NiSx layer resulting in a negligible concentration polarization. In the presence of an active flow, as in the case of the present work, the resistance in the gas phase is even less limiting.

- The formation of Ni_3S_2 layer has been modelled as a lumped pseudo first order reaction:

$$R = k_1 \cdot c^{R}_{H_2S}(x,t)$$

In which R is the reaction rate and k_1 is the pseudo first order kinetic coefficient.

- The layer of Ni_3S_2 is thin (no accumulation of H_2S in the porous layer i.e. thin film approximation), however the thickness of the film will still increase with time. This assumption means that the change in H_2S concentration at the interface are instantaneous when the concentration in the bulk changes:
  $$N''_{H_2S} = \frac{D_{H_2S-NiSx}}{\delta(x,t)} \cdot \left(c^{int}_{H_2S}(x,t) - c^{R}_{H_2S}(x,t)\right) = k_1 \cdot c^{R}_{H_2S}(x,t) \cdot P$$
  Where P is the specific area and lumps together also the reaction's stoichiometry:
  $P = S_v \cdot A_G/\nu$
  with $\nu = 2$ being the H_2S stochiometric coefficient and S_V and A_G are the surface area per unit volume of the Ni foam (usually measured or calculated in cm^2/cm^3, see [2]) and the cross sectional area of the capillary, respectively.
- The system of PDEs is solved as a semi-infinite medium, thus the right-hand side of the boundary conditions are at $x \to \infty$.

With those assumptions the governing equation system reads as:

Flux equation (defined on the thickness of the layer):

$$\frac{\partial \delta(x,t)}{\partial t} = \frac{M_{NiSx}}{\rho_{NiSx}} \cdot c_{H_2S}(x,t) \cdot \frac{1}{\frac{1}{k_1 \cdot P} + \frac{1}{D_{H_2S-NiSx}} \cdot \delta(x,t)}$$

$$\delta(0,t) = 0 \qquad x = 0 \; \forall t > 0$$
$$\lim_{x\to\infty} \delta(x,t) = 0 \qquad x \to \infty \; \forall t > 0$$
$$\delta(x,0) = 0 \qquad x \in [0,\infty) \;\; t = 0$$

Where M_{NiSx} and ρ_{NiSx} are the molecular weight and density of Ni_3S_2.

Balance equation:

$$\frac{\partial c_{H_2S}(x,t)}{\partial x} = -\frac{c_{H_2S}(x,t)}{V} \cdot P \cdot \frac{1}{\frac{1}{k_1 \cdot P} + \frac{1}{D_{H_2S-NiSx}} \cdot \delta(x,t)}$$

$$c_{H_2S}(0,t) = c^{in}_{H_2S} \qquad x = 0 \; \forall t > 0$$
$$\lim_{x\to\infty} c_{H_2S}(x,t) = 0 \qquad x \to \infty \; \forall t > 0$$
$$c_{H_2S}(x,0) = 0 \qquad x \in [0,\infty) \;\; t = 0$$

V is the volumetric flow and $c^{in}_{H_2S}$ is the inlet H_2S concentration. In the PDEs above, the adjustable parameters are $k^{T_{ref}}_1$, E_a, $D^{T_{ref}}_{H_2S-NiSx}$, $E_{a,D}$, and P.

The Ni_3S_2 weight faction, $WF_{NiS_x}\%$, is then calculated with the following equations, which take into consideration the stoichiometry of the reaction:

$$WF_{NiS_x}\%(x,t) = \frac{m_{NiS_x}(x,t)}{m_{NiS_x}(x,t) + m_{Ni}(x,t)} \cdot 100$$

Where the mass of Ni_3S_2 is calculated as

$$m_{NiS_x}(x,t) = \delta(x,t) \cdot A_{Ni} \cdot \rho_{NiS_X}$$

And the mass of Ni as:

$$m_{Ni}(x,t) = m_{Ni}(x,0) - \delta(x,t) \cdot A_{Ni} \cdot \rho_{NiS_X} \cdot 3\frac{M_{Ni}}{M_{NiS_X}}$$

Where M_{Ni} is the molecular weight of Ni and $m_{Ni}(x,0)$ is the initial mass of Ni.

Temperature dependence: The temperature dependence of both k_1 and $D_{H_2S-NiSx}$ is assumed to follow an Arrhenius-type correlation:

$$k_1 = k_1^{T_{ref}} \cdot \exp\left(-\frac{E_a}{R} \cdot \left(\frac{1}{T} - \frac{1}{T_{ref}}\right)\right)$$

$$D_{H_2S-NiSx} = D_{H_2S-NiSx}^{T_{ref}} \cdot \exp\left(-\frac{E_{a,D}}{R} \cdot \left(\frac{1}{T} - \frac{1}{T_{ref}}\right)\right)$$

Where $T_{ref} = 25\ °C$ is the reference temperature.

Data fitting and results

The table below reports the geometrical and physical-chemical parameters used.

Table S2. Overview of the geometrical and physical-chemical parameters used to interpret the experimental data.

Parameter	Value
Temperature	$T = 90 - 170\ °C$
Pressure	$p = 1$ atm
Capillary length	$L = 5$ mm
Integration time	$t = 3600$ s
Volumetric flow	$\dot{V} = 0.1 - 5\ NmL/min$
H_2S molar fraction inlet	$X_{H_2S} = 0.03$
Density Ni_3S_2	$\rho_{NiS_x} = 5800\ kg\ m^{-3}$
Density Ni	$\rho_{Ni} = 8900\ kg\ m^{-3}$
Ni_3S_2 molecular weight	$M_{NiSx} = 40.21\ g/mol$
Ni molecular weight	$M_{Ni} = 58.72\ g/mol$

While the parameters ($k_1^{T_{ref}}$, E_a, $D_{H_2S-NiSx}^{T_{ref}}$, $E_{a,D}$, and P) can all be optimized simultaneously with the e.g. the Simplex-method, the high dimensionality of the optimization space can result in a series of local minima for the error fitting function. Thus, some of the optimal sets of the parameters, while describing accurately

some set of experimental data, might not have physical meaning. Therefore, some parameters were taken as fixed to realistic values. In particular, the specific area was chosen to be $P = 0.24\ m$ (or 0.4 m^2/g) which is similar to the value reported for 110 PPI Ni-foam (1 m^2/g)[3] and inside the wide range reported in the literature for similar Ni foams (approx.: 0.05 – 5 m^2/g).[4,5]

The value for the activation energy of the diffusion coefficient, was fixed to $E_{a,D} =$ 40 kJ/mol which is inside the wide range reported for O_2 diffusion in SiO_2 layers (28 – 120 kJ/mol).[6] Here we note that we have performed sensitivity analysis on the value of the activation energy for the diffusion coefficient, and the results on the value of k_1 are basically unaffected from the choice of $E_{a,D}$ in a large range of $E_{a,D} \in [10,60]$ kJ/mol.

Therefore, the Nelder–Mead optimization algorithm was used to find the optimal subset of the model parameters: $k_1^{T_{ref}}$, E_a, and $D_{H_2S-NiSx}^{T_{ref}}$.

Standard errors and confidence intervals: The standard errors and the confidence intervals for each variable were calculated starting from the Jacobian matrix. The computational Jacobian matrix, J (size $n \cdot p$ with n is the number of experimental observations and p is the number of parameters) was constructed calculating the numerical derivatives around the optimized set of $\bar{x}$ (namely $k_{1,opt}^{T_{ref}}$ and $E_{a,opt}$) for each experimental observation: I.e. the Jacobian matrix reads as:

$$J = \begin{bmatrix} \left.\frac{\partial WF\left(k_1^{T_{ref}}, E_a\right)}{\partial k_1^{T_{ref}}}\right|_{\bar{x}, t_1} & \left.\frac{\partial WF\left(k_1^{T_{ref}}, E_a\right)}{\partial E_a}\right|_{\bar{x}, t_1} \\ \dots & \dots \\ \left.\frac{\partial WF\left(k_1^{T_{ref}}, E_a\right)}{\partial k_1^{T_{ref}}}\right|_{\bar{x}, t_n} & \left.\frac{\partial WF\left(k_1^{T_{ref}}, E_a\right)}{\partial E_a}\right|_{\bar{x}, t_n} \end{bmatrix}$$

Where $t_1,\dots,t_n$ are all the experimental observations at all the temperatures. Next, the standard error at $x = \bar{x}$ was computed as:

$$\left(J^T \cdot J\right)^{-1}\hat{\sigma}^2 = \begin{bmatrix} var\left(k_1^{T_{ref}}\right) & \dots \\ \dots & var\left(E_a\right) \end{bmatrix}$$

With the variance estimate $\hat{\sigma}^2$ defined as:

$$\hat{\sigma}^2 = \frac{1}{n-p}\sum_{j=1}^{q}\sum_{i=1}^{n}\left(WF_j(t_i,\bar{x}) - WF_{j,exp}(t_i)\right)^2$$

and the standard error for the parameter x_i being:

$$se(x_i) = \left[var(x_i)\right]^{\frac{1}{2}}$$

Finally, the 95% confidence interval for each parameter was calculated from the t-student function as:

$95\%\ CI_i = \bar{x} \pm t(0.975, n-p) \cdot se(x_i)$

The final fitting parameters found are reported in the table below.

Table S3. Optimized set of parameters and standard errors obtained by the fitting of the weight fractions by fixing $P = 0.24\ m$ and $E_{a,D} =$ 40 kJ/mol.

Parameter	Value
Diffusion coefficient H_2S porous Ni	$D^{T_{ref}}_{H_2S-NiSx} = 2 \cdot 10^{-13}\ m^2/s$
Kinetic pseudo-first order	$k^{T_{ref}}_{1} = (3.4 \pm 0.1) \cdot 10^{-8} 1/s$
Activation energy kinetic	$E_a = 65.3\ \pm 0.3 \frac{kJ}{mol}$

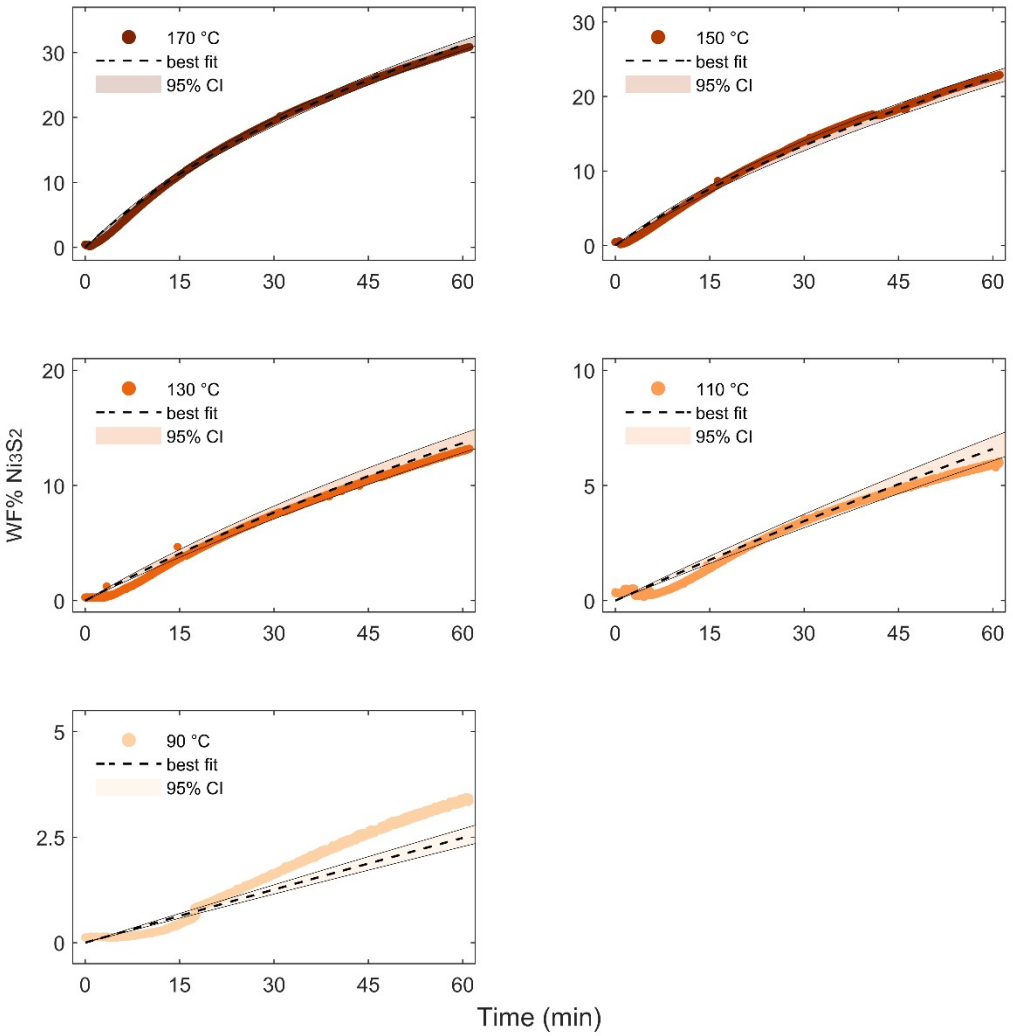

Figure S10 95% confidence intervals (CI) for the fitting reported in Figure 3(a) in the main manuscript..

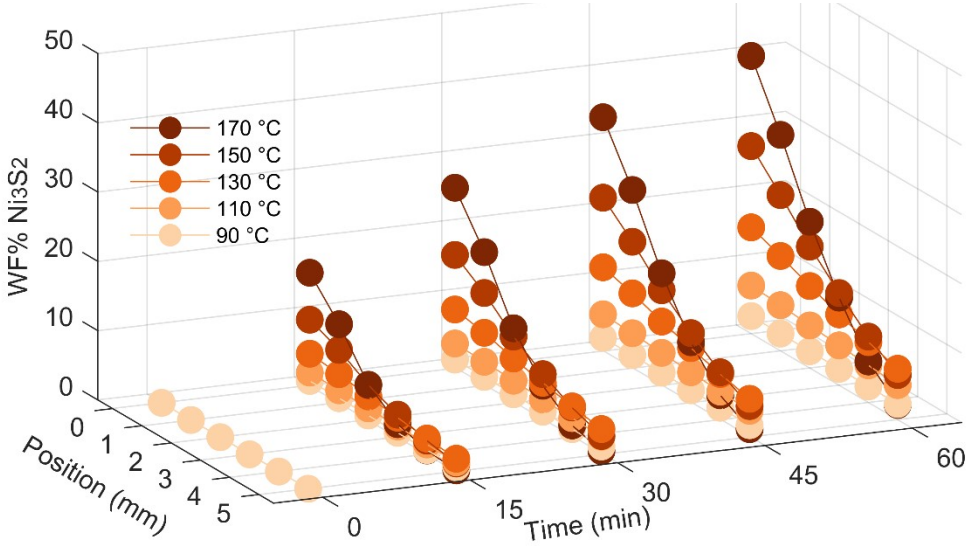

Figure S11 Model simulations of the NiS_x growth versus temperature and position.

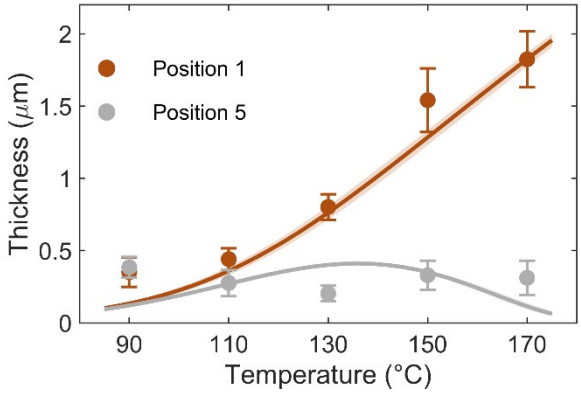

Figure S12 Model simulations of the temperature dependence of the NiS_x thickness.

Influence of the Ni_3S_2 layer resistance

When the reaction between H_2S and Ni is approximated to a pseudo-first order reaction, and considering the hypothesis of thin film (no accumulation of H_2S in the porous Ni_3S_2 layer) the relative influence of the resistance for the reaction over the total resistance can be simply expressed as:

$$\phi = \frac{1}{1+\frac{k_1 \cdot P}{h_m}} = \frac{1}{1+\frac{k_1 \cdot P}{D_{H_2S-NiSx}} \cdot \delta(x,t)}$$

At high values of ϕ, the system is reaction-limited, at low value of ϕ the system becomes diffusion-limited. Conversely, the resistance of the Ni_3S_2 layer is expressed as $1-\phi$. Figure S13 shows how the increase in temperature shifts the system from being controlled by the reaction to be controlled by diffusion. This is

due to the faster relative increase in the reaction kinetic with respect to the increase in the diffusion coefficient. Qualitatively this can also be seen in the time-profiles for the Ni_3S_2 weight fraction which becomes less linear with the increase in temperature. Here we note that if the system were fully controlled by diffusion, the time-dependency on the Ni_3S_2 thickness would be proportional to the square root of time, as typical of any diffusion-limited process.

With the set of parameters used, the highest temperatures (namely 150 °C and 170 °C) have an appreciable influence of the porous layer resistance at the end of the experiment (60 minutes) 57% and 73%, respectively; while at 130 °C there is a less evident, yet present, effect 47%. As clear from Figures S11-S13, also after just 15 minutes at the highest temperatures the system is partially controlled by diffusion. I.e. at 170 °C and 15 minutes the relative influence for diffusion in the Ni_3S_2 layer (~48%) is almost equal to the one from the reaction.

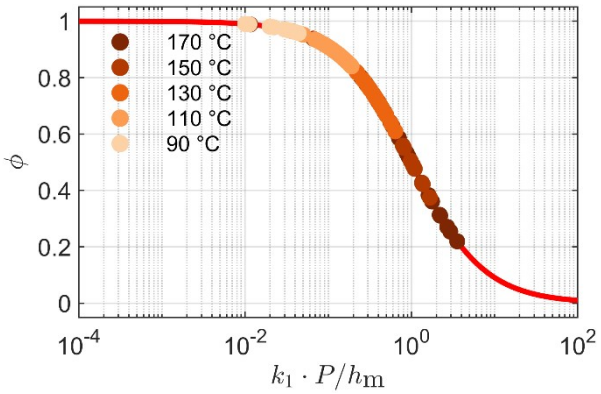

Figure S13 Calculated dimensionless resistance, ϕ, for all the experimental points reported in Figure 5a of the main text and Figure S9.

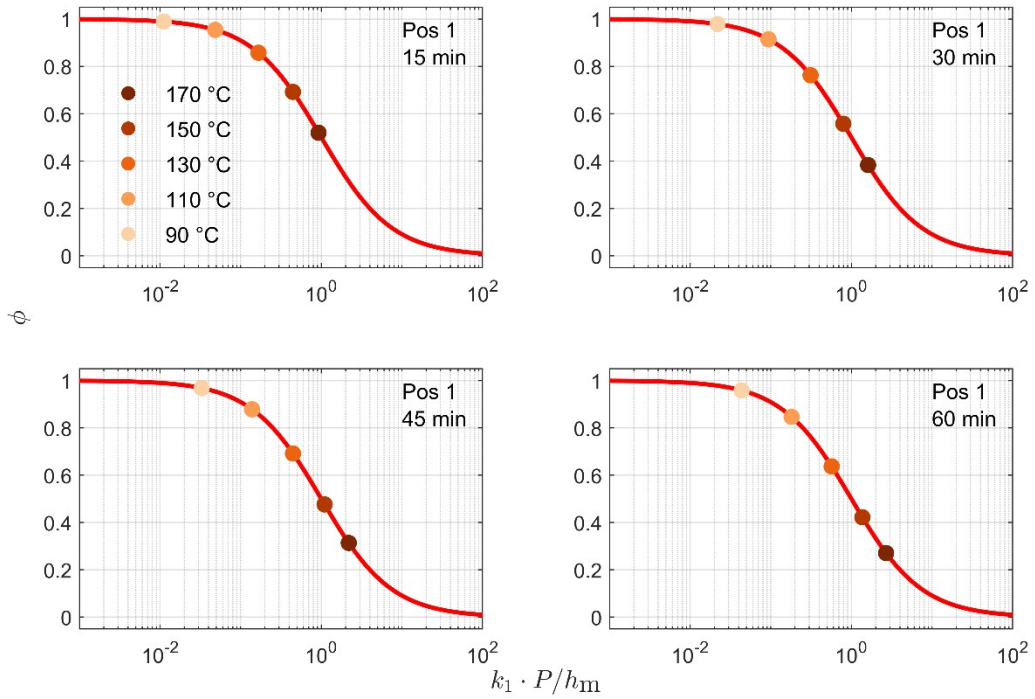

Figure S14 Calculated dimensionless resistance, ϕ, for position 1 at 15, 30, 45, and 60 minutes.

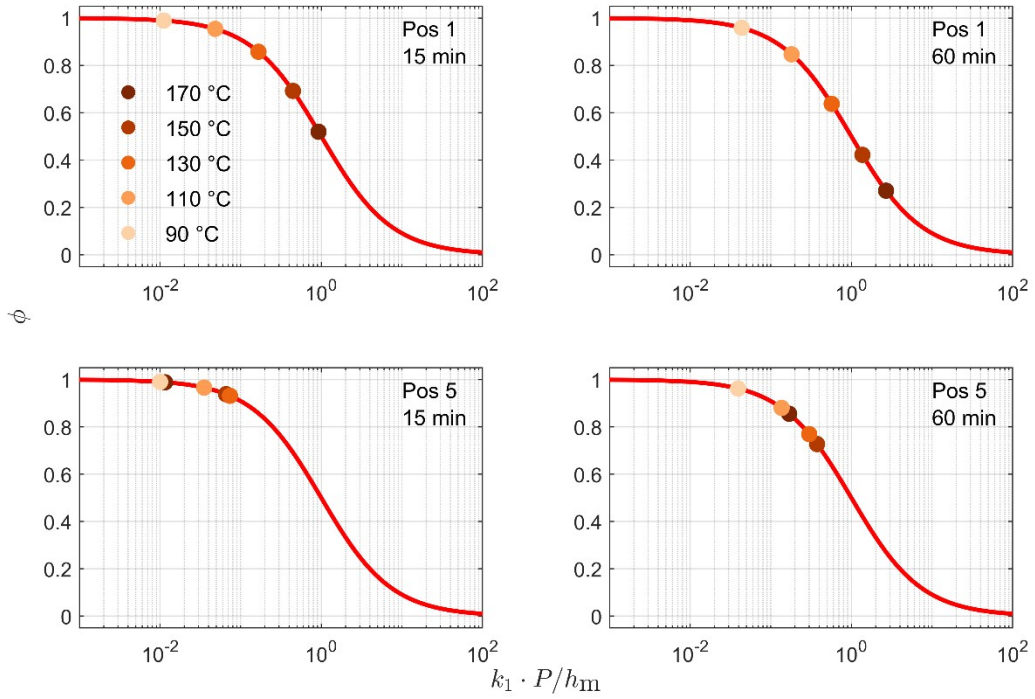

Figure S15 Calculated dimensionless resistance, ϕ, for position 1 and 5 at 15 and 60 minutes.

4. Reproducibility and flow series

The following section includes data collected and refined for three samples sulfided at the same conditions flow of 0.5 mL/min and temperature of 130 °C and the flow series at 130 °C from 0.1-5 mL/min. For the flow series, the raw PXRD pattern is found in figure S16, and the WF% of Ni_3S_2 in figure S17 together with the modelled data. The raw PXRD pattern as heatmap for position 1 as a function of time is found in Figure S18. The WF% of Ni_3S_2 as a function of time from the Rietveld refinement in Figure S19(a). The WF% of Ni_3S_2 after synthesis as a function of position of the Rietveld refinement in Figure S19(b). Both figures in Figure S19 show good reproducibility. The raw diffractograms are shown after 1 h of synthesis in Figure S20. This figure shows that the replica S3 has some peaks, which are not described, thus, the sample S3 is not used in the kinetics estimation. Figure S21 presents the sulphur concentration in the outlet for samples synthesised at 0.5 mL/min and 5 mL/min.

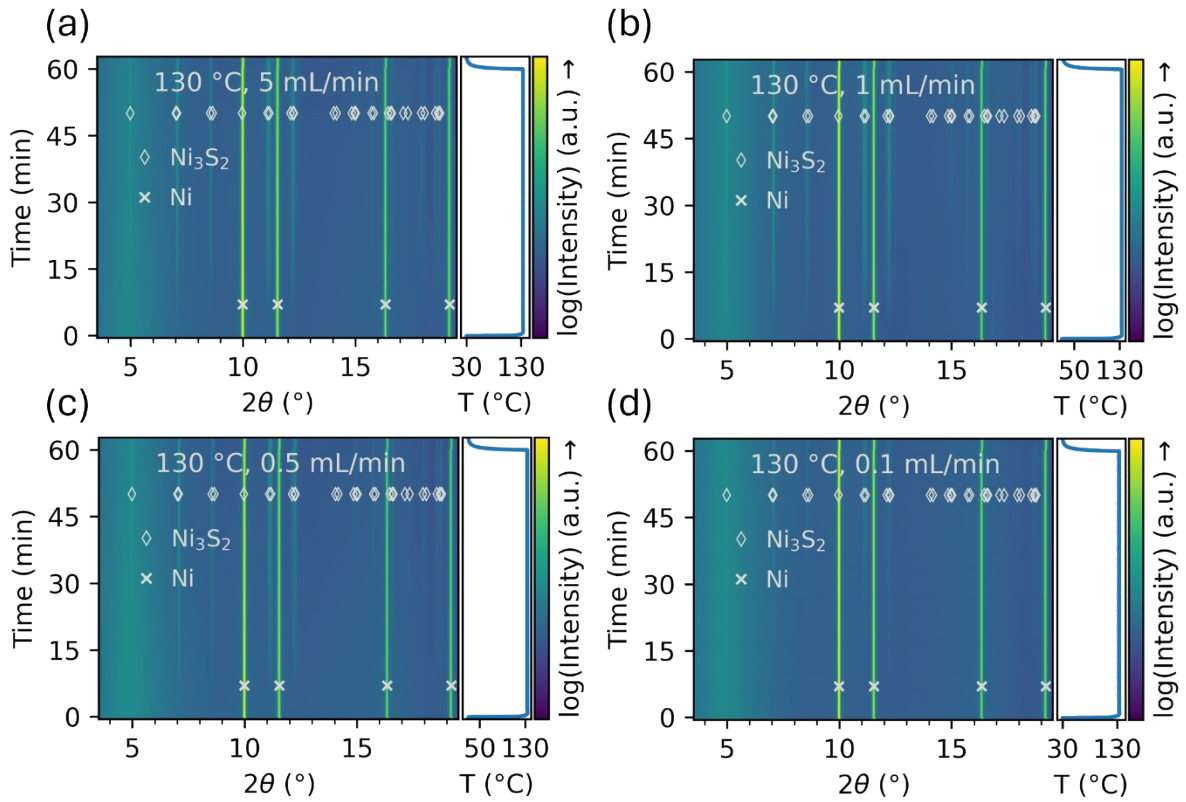

Figure S16 PXRD patterns as a function of time for samples 130 °C at different temperatures at position 1 from the H_2S inlet for samples (a) 5 mL/min, (b) 1 mL/min, (c) 0.5 mL/min, and (d) 0.1 mL/min.

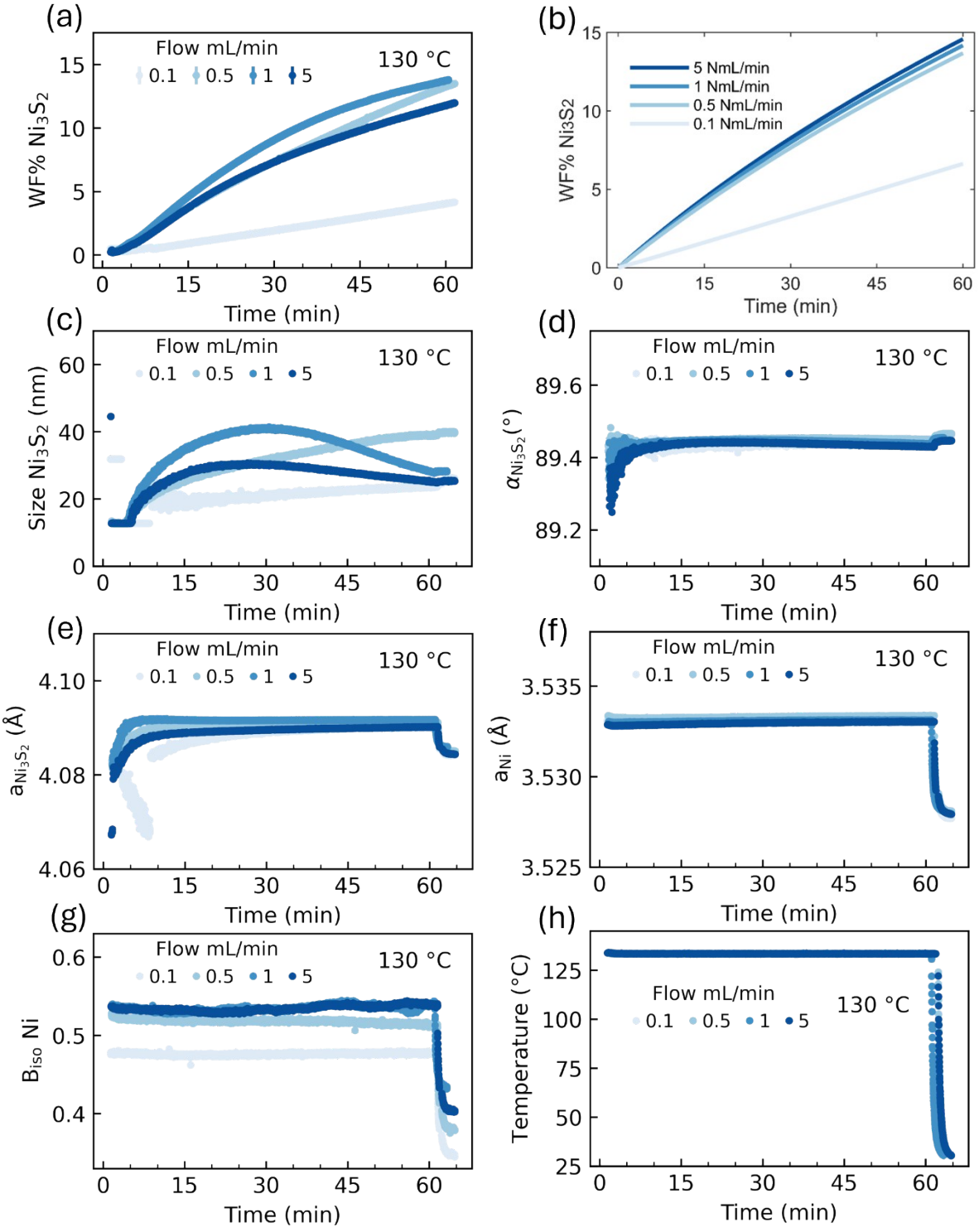

Figure S17 Weight fraction of Ni_3S_2 for samples 130 °C at different flow from 0.1-5 mL/min at position 1. (a) Real data and (b) model simulations. Obtained values from sequential Rietveld refinements for samples at temperatures 130 °C and flowrates 0.1-5 mL/min. The Rietveld refinements are performed on data collected at position 1. (c) Crystallite sizes of Ni_3S_2, however, this could also be refined as strain (d) α of Ni_3S_2, (e) Unit cell parameter of Ni_3S_2, (f) unit cell parameter of Ni, (g) Isotropic B-values for Ni, and (g) the development in temperature during the experiments.

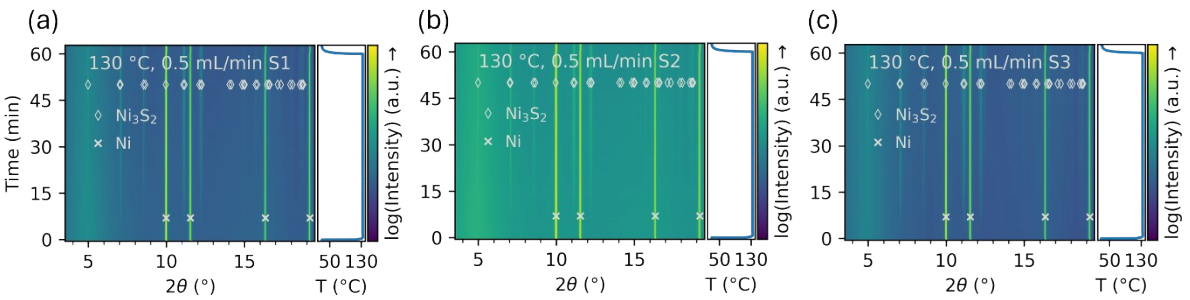

Figure S18 PXRD patterns as a function of time for samples 130 °C at different temperatures at position 1 from the H_2S inlet for samples (a) 0.5 mL/min, (b) 0.5 mL/min v2, and (c) 0.5 mL/min v3

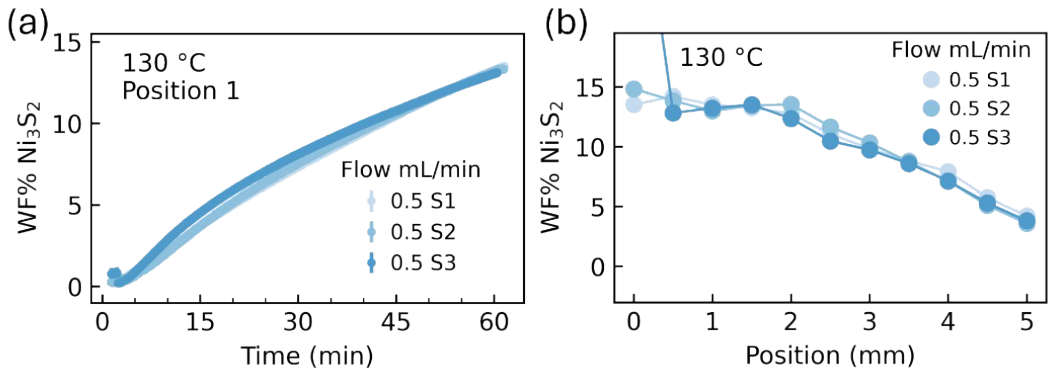

Figure S19 Three samples synthesized with a flow of 0.5 mL/min, 130 °C with (a) Weight fraction of Ni_3S_2 as a function of time. (b) Weight fraction of Ni_3S_2 after synthesis as a function of position on the sample.

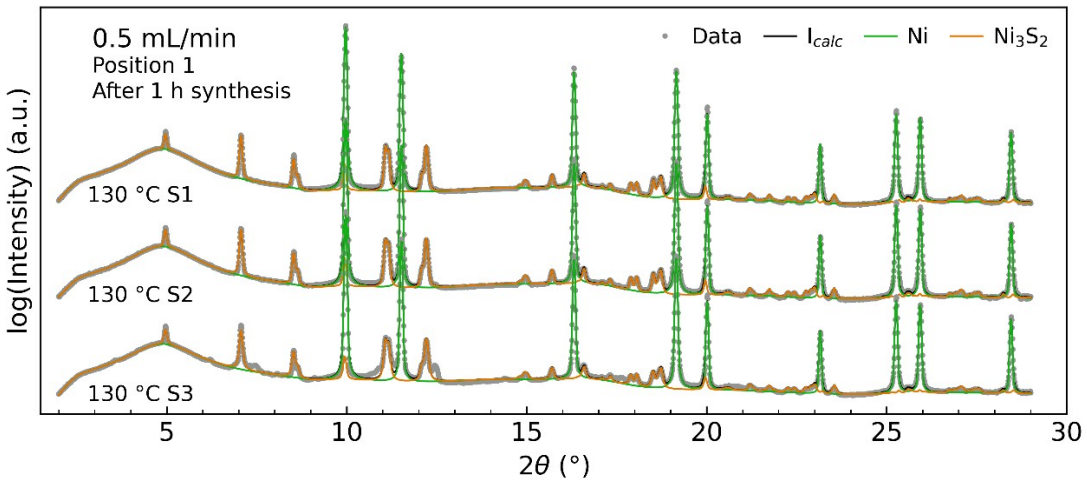

Figure S20 Diffractogram of three samples with flow of 0.5 mL/min at 130 °C after a reaction time of 1 h from position 1 with Rietveld refinement of phase Ni in green and Ni_3S_2 in orange.

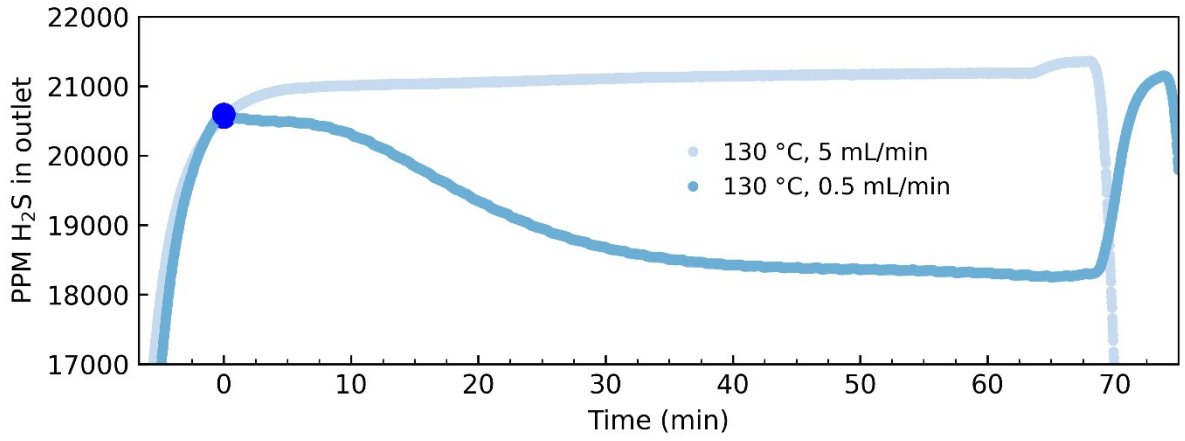

Figure S21 SulfiLogger sensor measuring PPM H_2S in outlet for 130 °C samples at 5 mL/min and 0.5 mL/min. Blue dots indicate the onset of heating. While the absolute ppm values are approximate due to the sensor not being calibrated for such low flow rates, the data still effectively illustrate the overall trend.

5. Lateral position in temperature series

The following section presents data collected for the temperature series at 90–170 °C, measured across lateral positions. During synthesis, lateral position measurements were taken at six points over a 5 mm range every 15 minutes. Before and after synthesis, measurements were taken at 11 points over the same 5 mm range.

The raw PXRD pattern obtained after synthesis of the temperature series at 0.5 mL/min is presented as a heatmap for positions 0 to 5 in Figure S22. The WF% of Ni_3S_2 after synthesis, as a function of position on the sample, is shown for 0.5 mL/min and 1 mL/min in Figure S23(a) and (b), respectively. Figure S23(a-b) demonstrates that across all temperatures, higher flow rates lead to a more uniform distribution of Ni_3S_2. Figure S24 shows the normalised atomic percentage of sulphur, derived from EDX analysis at positions 1 and 5, as a function of synthesis temperature for 0.5 mL/min samples. The normalised atomic percentage of sulphur ranges between 20% and 45%, with some variation expected, as measurements were conducted at a single spot. Additionally, no sulphur content was detected in the sample synthesised at 70 °C. Figure S25 presents the sulphur concentration in the outlet for samples synthesised at 0.5 mL/min and temperatures of 110 °C, 130 °C, and 170 °C, recorded throughout the synthesis process. The data indicate an excess of hydrogen sulphide in the outlet, even at the higher temperature of 170 °C.

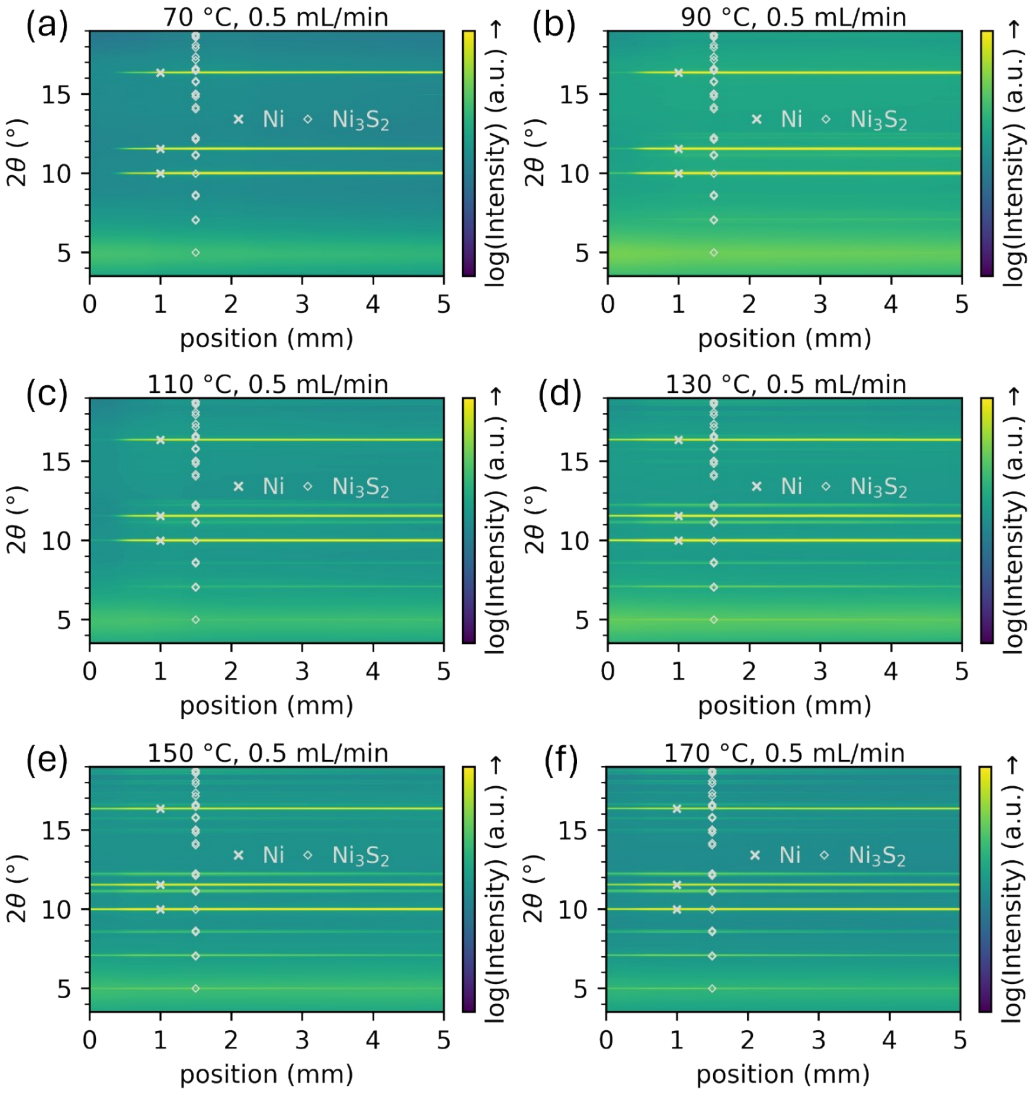

Figure S22 PXRD patterns as a function of position and color as a function of log(Intensity) for samples 0.5 mL/min after synthesis at different temperatures: (a) 70 °C, (b) 90 °C, (c) 110 °C, (d) 130 °C, (e) 150 °C, and (f) 170 °C.

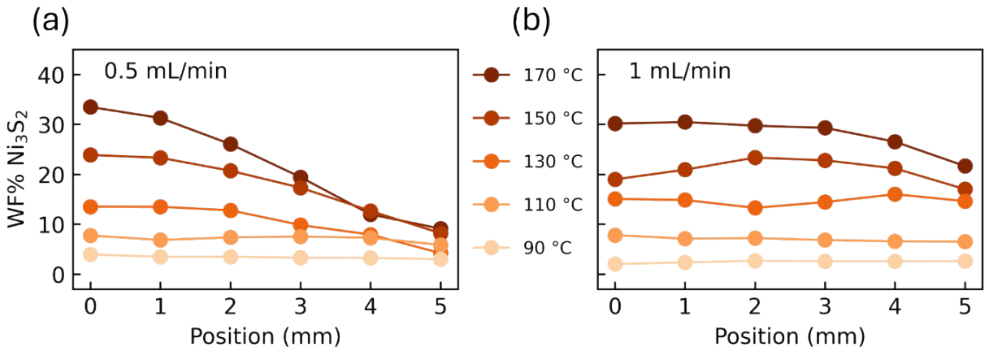

Figure S23 Weight fraction of the Ni_3S_2 phase as a function of the position on the sample after synthesis for 1 h for (a) 0.5 mL/min and (b) 1 mL/min.

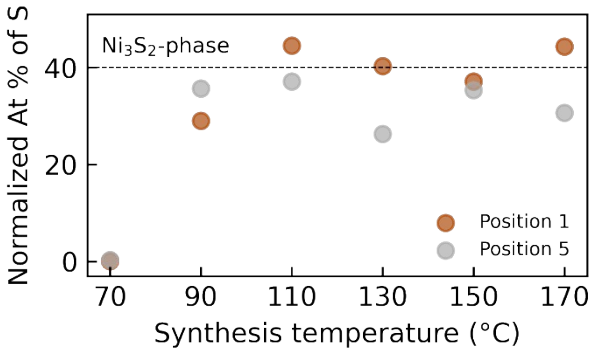

Figure S24 EDX values for the 0.5 mL/min samples from one spot magnification of 37 kx and FoV of 15 µm, At% values of S are normalized to the At% of Ni.

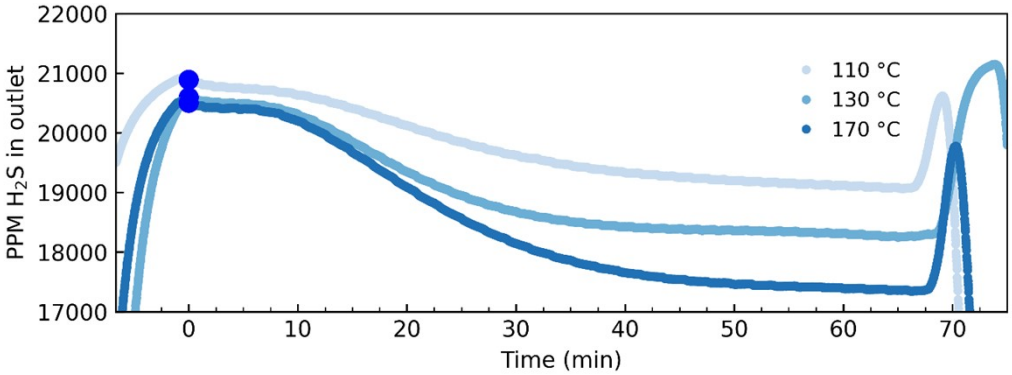

Figure S25 SulfiLogger sensor measuring PPM H_2S in outlet for 0.5 mL/min samples at 110 °C, 130 °C, and 170 °C. Blue dots indicate the onset of heating. While the absolute ppm values are approximate due to the sensor not being calibrated for such low flow rates, the data still effectively illustrate the overall trend.

6. Examination of additional phases

This section examines the additional phases identified in the diffractograms across the lateral positions on the sample. It begins by showing the diffractograms for the temperature series at 0.5 mL/min after 1 hour of synthesis, specifically at position 1, as shown in Figure S26. The figure reveals the samples synthesized at low temperature exhibit peaks at 2θ = 7.5° and 2θ = 12.48°, which cannot be attributed to the Ni or Ni_3S_2 phases. Similarly, for the flow series at higher flow rates of 1 and 5 mL/min, the same characteristic peaks are observed, as illustrated in Figure S26. Literature reports that Ni_3S_2, is not the most thermodynamically stable and NiS and Ni_7S_6 is more stable.[7,8] To investigate the unknown peaks, diffractograms from sample 90 °C was analysed further in section 6.1. However, no nickel-sulphide phase was found that matched the observed peaks. Thus, to examine how the unknow phase is distributed in the lateral position, single peak fitting was made in figure 6 and briefly explained in Section 6.2

For the high-temperature samples in Figure S26, additional unexplained peaks are also evident. These are attributed to the NiS millerite phase, as discussed in section 6.3.

SEM images of the peaks at position 0-1 for the 0.5 mL/min temperature series are presented in Figure S28. These images demonstrate an increase in peak size with rising temperature. Finally, SEM images and photographs of the entire nickel foam are shown in Figure S29, highlighting a decrease in the number of extrusions at the outlet as the temperature increases. In the main article, it is hypothesized that the extrusions could be related to the additional peaks in the diffractogram.

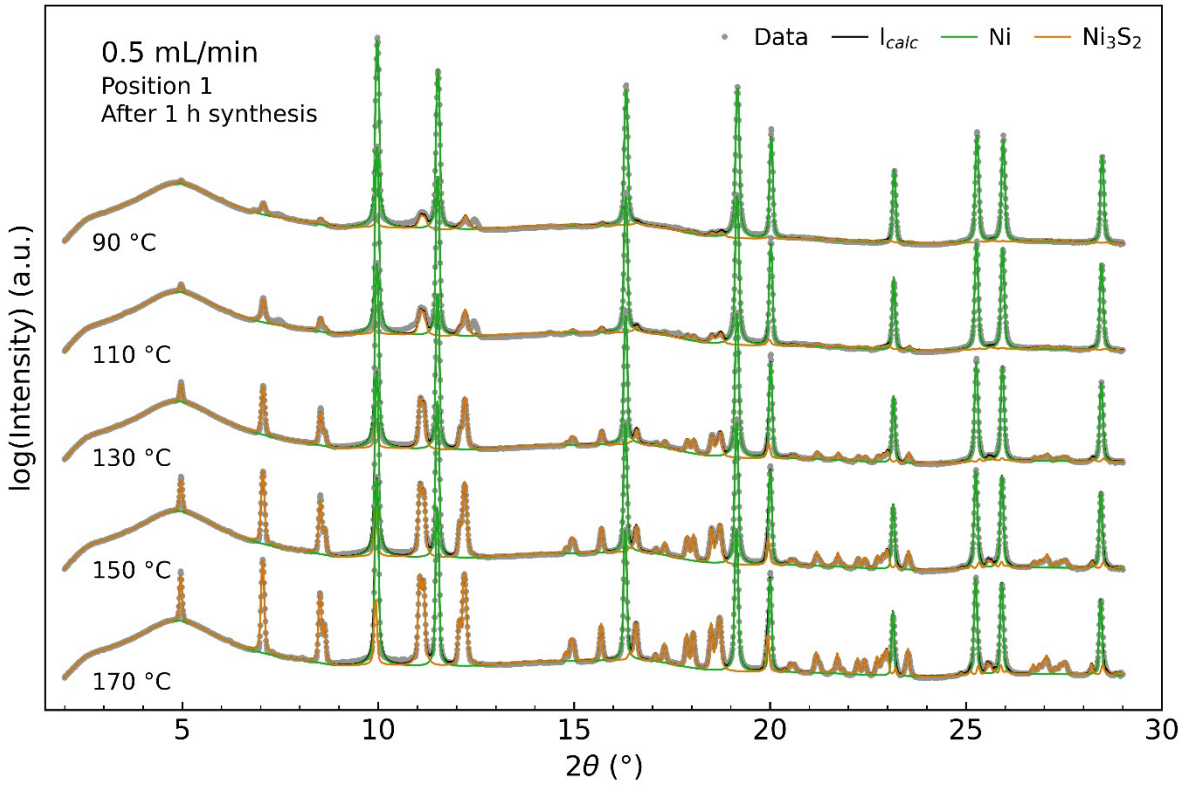

Figure S26 Diffractogram of samples with flow of 0.5 mL/min at 90-170 °C after a reaction time of 1 h from position 1 with Rietveld refinement of phase Ni in green and Ni_3S_2 in orange.

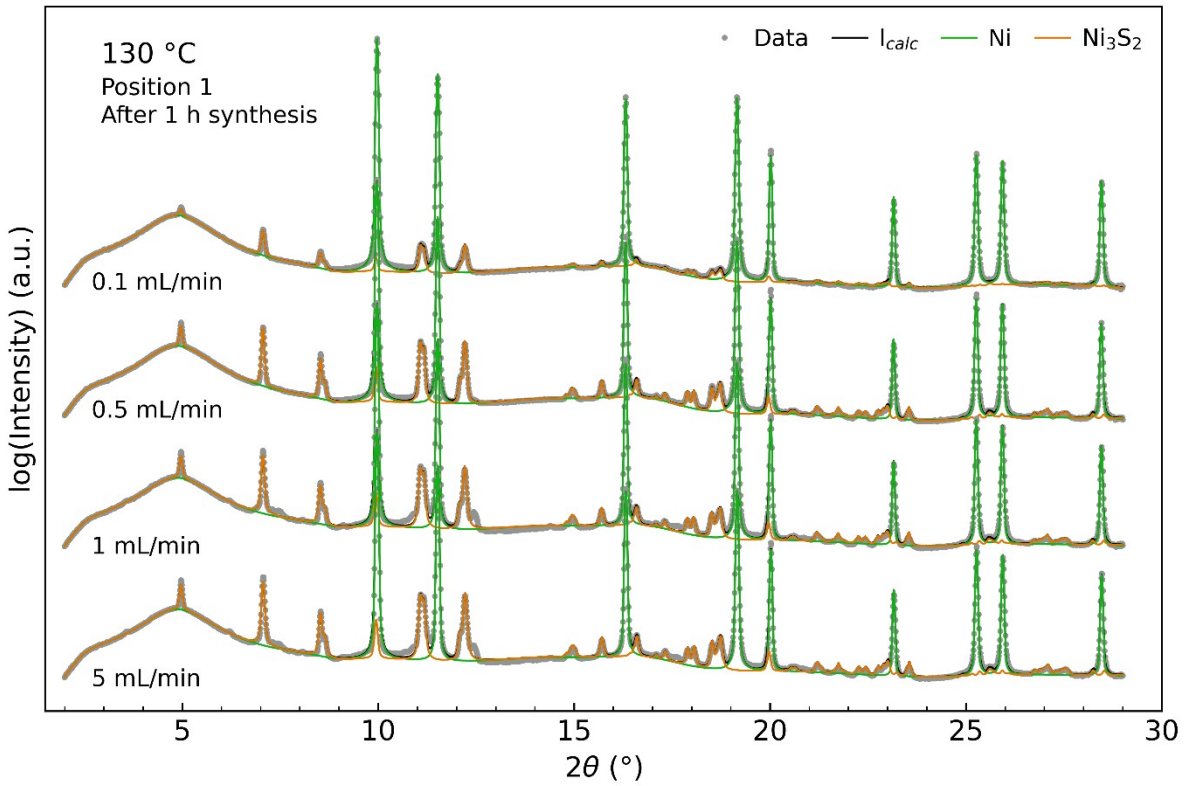

Figure S27 Diffractogram of samples made at 130 °C with flow of 0.1-5 mL/min position 1 after a reaction time of 30 min in black and 60 min in grey and refined Ni_3S_2 phase after 60 min in orange.

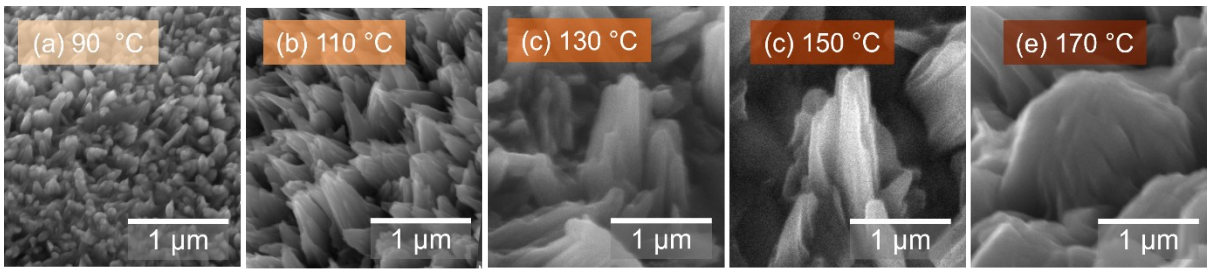

Figure S28 SEM images of spikes from position between 0 and 1 for 0.5 mL/min samples with reaction temperatures of (a) 90 °C, (b) 110 °C, (c) 130 °C, (d) 150 °C, and (e) 170 °C

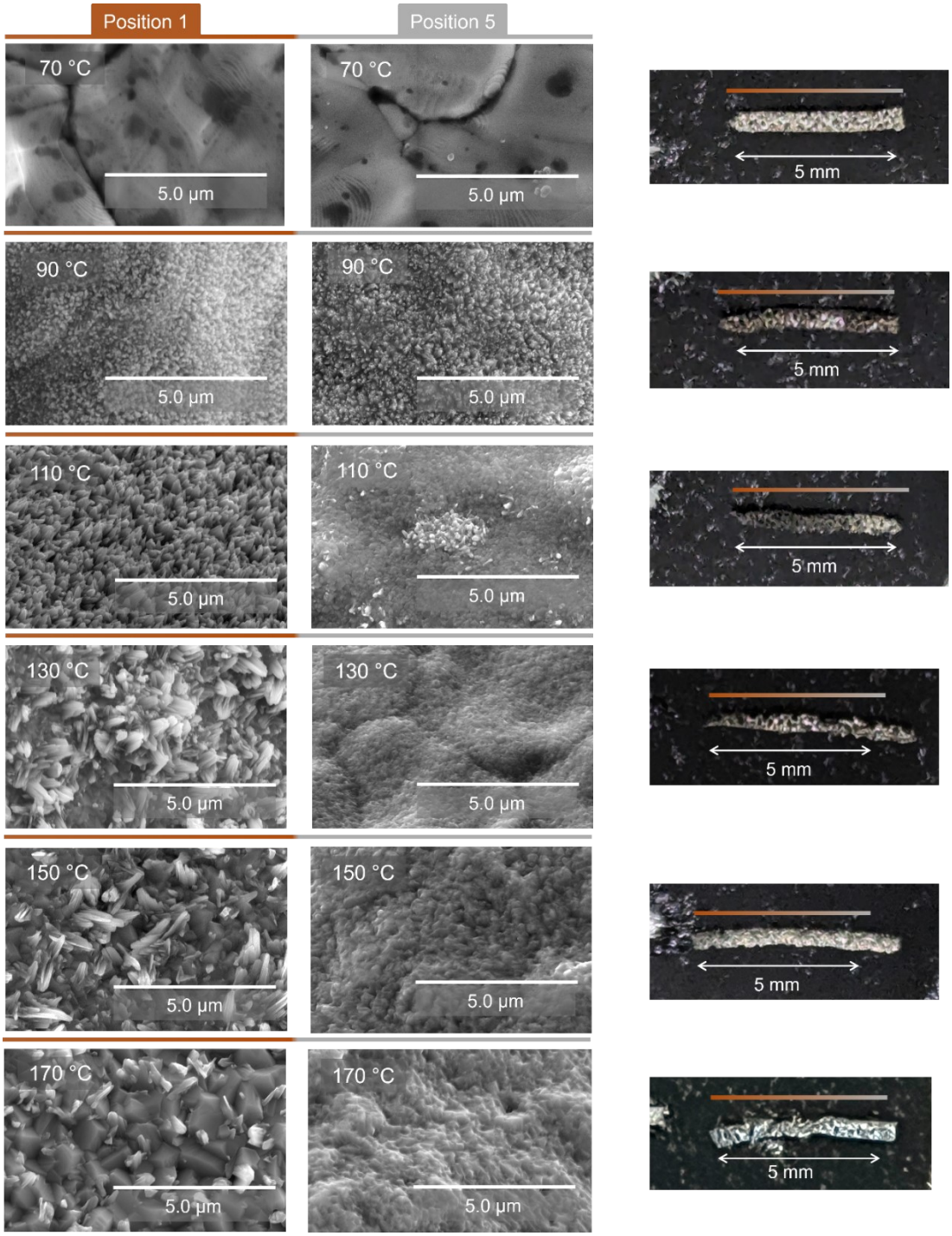

Figure S29 SEM images of position 1 and 5 for samples 0.5 mL/min at all temperatures, and pictures of the Ni-foam after the synthesis with inlet side pointing to the left.

6.1 Examination of additional phase in 90 °C

There is a significant peak at 2θ = 7.45° and 2θ = 12.48° for samples 90 °C, 0.5 mL/min and 110 °C, 0.5 mL/min, which is not described by Ni or Ni_3S_2, as seen in figure S26. This phase was examined more in depth by examination of other possible NiS_x-phases. Among others, the following phases were refined on sample 90 °C, 0.5 mL/min after synthesis at position 2, where the undescribed peaks are most predominant. Phases including the following phases found in COD and ICSD databases:

Ni_7S_6 Godlevskite (B m m b, ICSD 2768),[9]

Ni_9S_8 Godlevskite (I -4 2 d, COD 9013880),[10]

NiS millerite (R 3 m H, ICSD 40054),[11]

NiS Nickeline (P 63 m c, ICSD 42494),[12]

Ni_3S_4 Polydymite (F d -3 m, COD 9009863),[13]

NiS_2 Pyrite (P a -3, ICSD 198103)[14]

The background was refined at position 2 before synthesis and set constant for the refinements that were made after synthesis and cooling of the sample. For the refinements shown in Figure S30, the minimum size was set to 12.7 nm, and the unit cell parameters a, b, and c were kept constant at the values originally reported for the structure. The scale was set to a minimum to be able to visualize the phase, thus, the WF% has no real meaning in table S3. As seen from figure S30, there are no obvious best fits for the extra phases. The Ni_7S_6 phase has a peak at 2θ = 12.48°, however, it has peaks just above 2θ = 8° and 2θ = 17° which is not present in the experimental data, clearly indicating that this is not the missing phase.

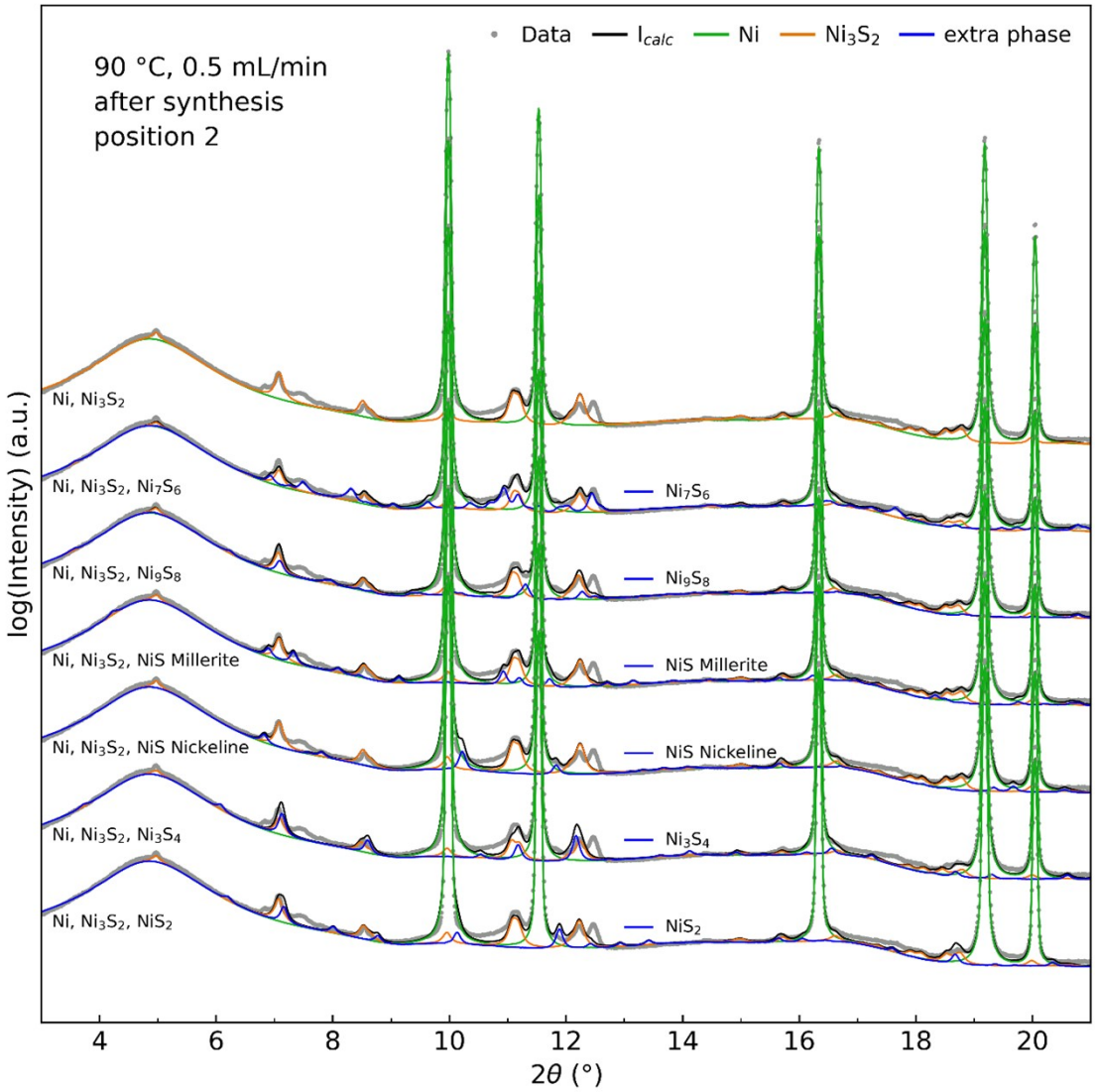

Figure S30 Rietveld refinements of different phases in 90 °C, 0.5 mL/min position 2 after synthesis. Values obtained are found in table S4.

Anisotropic broadening considerations

Given the nature of the H_2S reaction happening on the surface, it is likely that the extra phase is a thin film with highly preferential growth direction. This would skew the diffraction pattern heavily, effectively mimicking anisotropic crystallites sizes, resulting in variations in broadening across Bragg reflections. The phases were refined using an anisotropic particle size in Topas. Initially, different directions such as (100), (110), (111), and (001) were tested for obvious matches in the direction of anisotropic broadening. If these did not yield reasonable results, the unit cell parameters a, b, and c were refined to align the peak at 2θ = 12.48°. The miller indices of the peak were then identified, and the anisotropic refinement was adjusted accordingly. The results are shown in Figure S31, and Table S4 lists the refined values, including lattice parameters (a, b, c), the anisotropic size (r_x , r_z), and a schematic of the resulting shape. The results from Figure S30 indicate that neither phase fits both missing peaks at 2θ=7.45° and 2θ = 12.48°, without introducing peaks, which are not present in the data. To point out the mismatch, Figure S32 is included with zooms of the anisotropic Rietveld refinement with phase Ni_7S_6, as it presents the best agreement with the data.

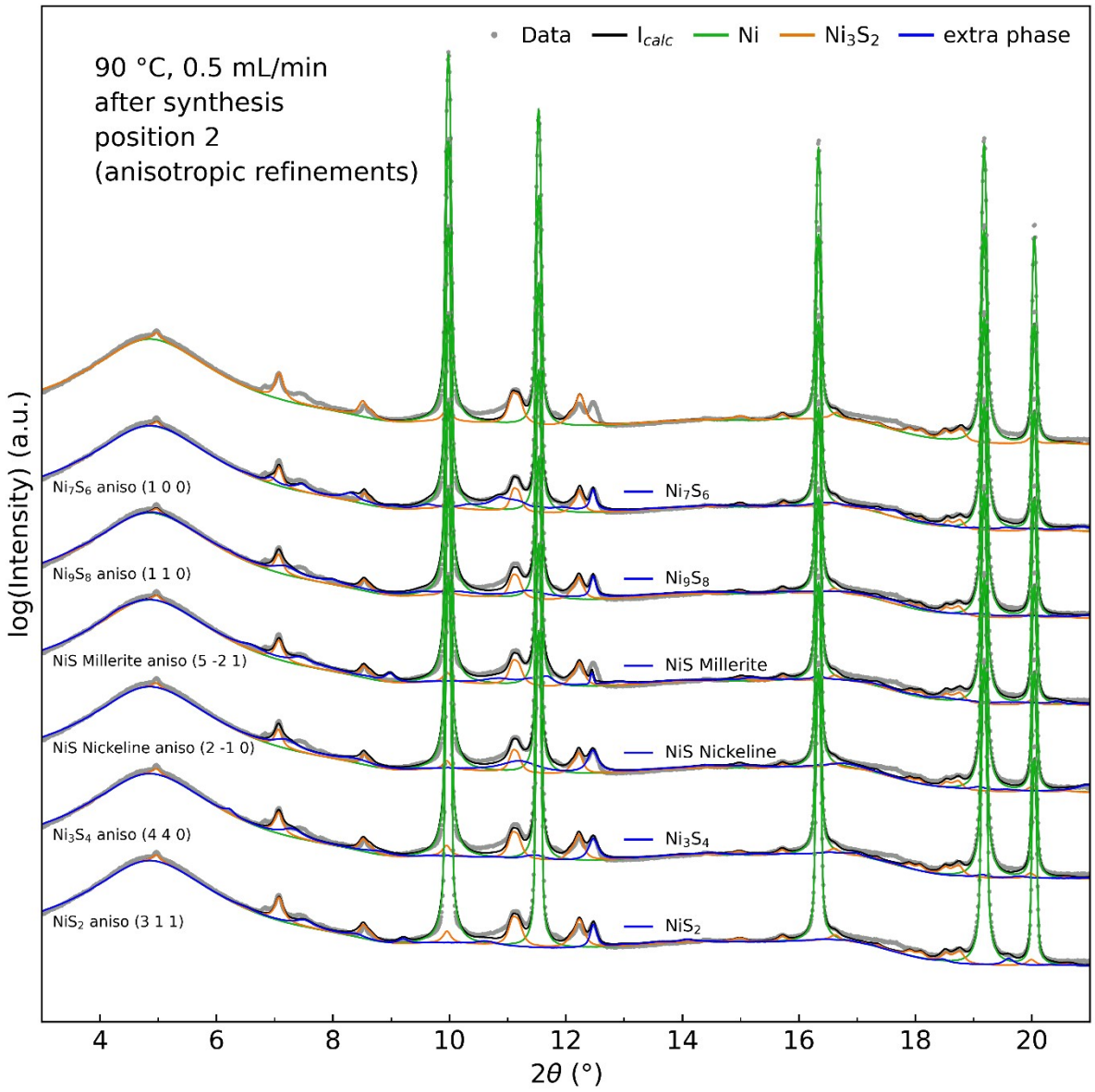

Figure S31 Rietveld refinements of 90 °C, 0.5 mL/min position 2 after synthesis with different phases using anisotropic size broadening. Values obtained are found in table S3.

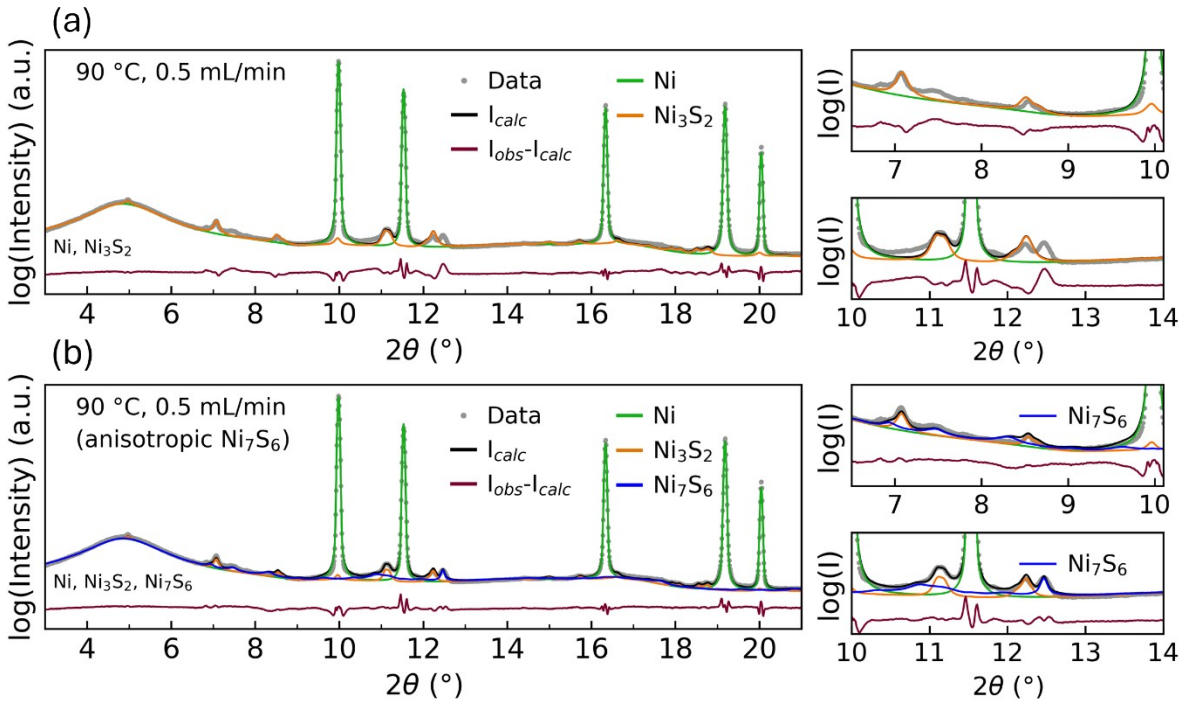

Figure S32 Rietveld refinements of 90 °C, 0.5 mL/min position 2 after synthesis with (a) Ni and Ni_3S_2 and (b) Ni, Ni_3S_2 Ni_7S_6 with anisotropic broadening.

Phases included	Extra phase	a, b, c	Size (nm)	WF%	Anisotropic direction	rx (nm)	ry (nm)	Anisotropic projection
Ni, Ni_3S_2	Ni_7S_6	3.274, 16.157, 11.359	12.7(2.4)	4.2(4)	-	-	-	-
Ni, Ni_3S_2	Ni_7S_6	3.264(2), 16.42(9), 11.21(6)	-	5.8(4)	(1 0 0)	1.3(2)	9(3)	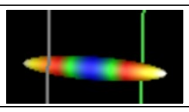
Ni, Ni_3S_2	Ni_9S_8	9.38, 9.38, 22.44	12.7(4.3)	1.8(3)	-	-	-	-
Ni, Ni_3S_2	Ni_9S_8	9.233(6), 9.233(6), 22.6(4)	-	4.2(4)	(1 1 0)	0.55(8)	8(2)	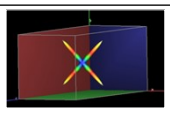
Ni, Ni_3S_2	NiS	9.6112, 9.6112, 3.1508	12.7(3.0)	0.8(1)	-	-	-	-
Ni, Ni_3S_2	NiS	9.45(2), 9.45(2), 3.32(2)	-	1.8(2)	(5 -2 1)	0.6(1)	1e4 (5e6)	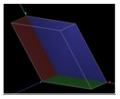
Ni, Ni_3S_2	NiS p63mc	3.4398, 3.4398, 5.3482	12.7(3.4)	1.1(2)	-	-	-	-
Ni, Ni_3S_2	NiS p63mc	3.265(3), 3.265(3), 4.73(3)	-	4.2(4)	(2 -1 0)	0.53(6)	2.7(4)	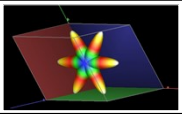
Ni, Ni_3S_2	Ni_3S_4	9.457, 9.457, 9.457,	12.7(2.3)	2.3(3)	-	-	-	-

Ni, Ni_3S_2	Ni_3S_4	9.230(8), 9.230(8), 9.230(8)	-	2.6(3)	(4 4 0)	0.7(1)	3.1(6)	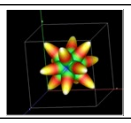
Ni, Ni_3S_2	NiS_2	5.677, 5.677, 5.677	12.7(2.6)	2.0(2)	-	-	-	-
Ni, Ni_3S_2	NiS_2	5.411(4), 5.411(4), 5.411(4)	-	2.3(3)	(3 1 1)	0.5(1)	5(1)	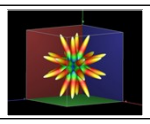

Table S4 Results of test of Rietveld refinements with different phases and different anisotropic directions for each phase to attempt to match the missing phase in 90 °C, 0.5 mL/min at position 2 after synthesis.

6.2 Single peak fitting in sample 90 °C, 110 °C and 130 °C

As the peaks at 2θ = 7.45° and 2θ = 12.48° was not attributed to a phase in Section 6.1, single peak fitting was made on the peaks in the range of 2θ from 11.95°-12.8°. The single peak was made with Gaussian distribution for each peak and a linear line describing the background. The equation for the gaussian peak is described below.

$$f(x) = a \cdot \ exp\left(-\frac{-(x\ -\ x0)^2}{2 \cdot \sigma^2}\right)$$

When fitting three peaks, the function, including the straight line fitted as background, looks like this:

$$f(x) = a_1 \cdot \ exp\left(-\frac{-(x\ -\ x_{01})^2}{2 \cdot \sigma_1^2}\right) + a_2 \cdot \ exp\left(-\frac{-(x\ -\ x_{02})^2}{2 \cdot \sigma_1^2}\right) + a_3 \cdot \ exp\left(-\frac{-(x\ -\ x_{03})^2}{2 \cdot \sigma_3^2}\right)$$

$$+\ m * x + b$$

6.3 Examination of additional phases in 150 °C and 170 °C samples

This subsection examines SEM of the inlet of H_2S of sample 170 °C and additional phases observed in the 150 °C and 170 °C samples for both 0.5 mL/min and 1 mL/min throughout the lateral position. Figure S29 reveals that the morphology at position 1 consists of extrusions on the surface whereas, position 5 is more planar. This is investigated more in-depth for sample 170 °C, 0.5 mL/min in Figure S33 showing SEM images of the position 0, and a position between 0 and 1. These SEM reveal that closer to position 0 in Figure S33(b) there is a significant morphology change with larger and more well-defined extrusions compared to the position closer to position 1 in Figure S33(c). A literature study reports that the layer with sulfiding below 670 °C will consist of a thick inner layer of Ni_3S_2 and a thin outer layer of NiS,[15,16] a theory could be that the larger extrusions at position 0 may correlate with the formation of a more sulphur-rich phase. Figure S34(a) displays the WF% of NiS Millerite as a function of position from the inlet, which is apparent in the 150 °C and 170 °C samples both at 1 mL/min and 0.5 mL/min. The WF% being between 1.5-3 % NiS Millerite at position 0. Additionally, the Ni_9S_8 phase was also observed for samples at 1 mL/min at 150 °C and 170 °C, shown in Figure S34(b). PXRD patterns of the 170 °C, 1 mL/min sample in Figure S35(a-b) shows the presence of NiS millerite and Ni_9S_8 phases. Literature suggests that NiS is more thermodynamically favourable compared to Ni_3S_2.[8]

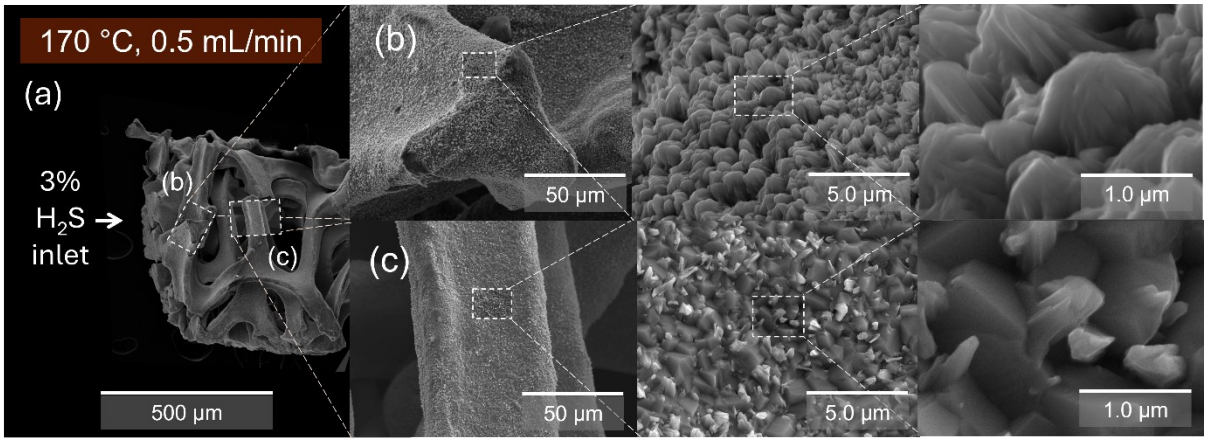

Figure S33 SEM images of sample 170 °C, 0.5 mL/min with (a) overview of the inlet side of the sulfided Ni foam, (b) SEM and magnifications at position 0, and (c) SEM and magnifications at position between position 0 and 1.

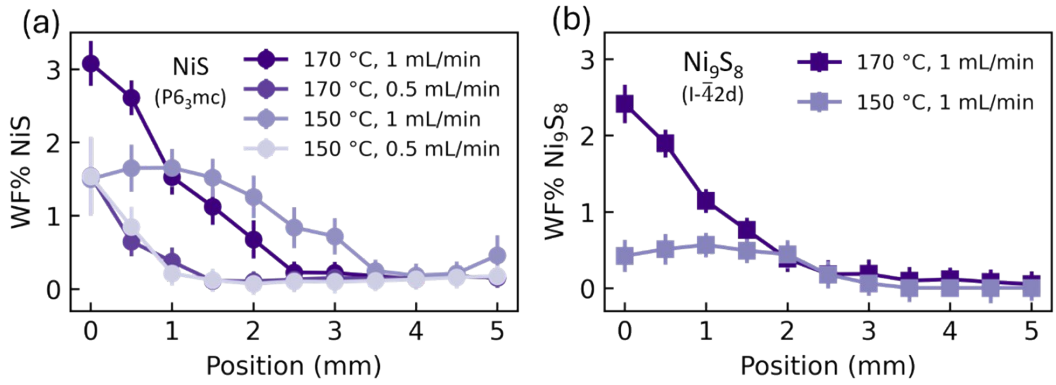

Figure S34 WF% of phases NiS Millerite[11] and Ni_9S_8 [10] observed for higher temperatures of 150 and 170 °C after 1 h synthesis as a function of sample position (a) NiS Millerite and (b) Ni_9S_8.

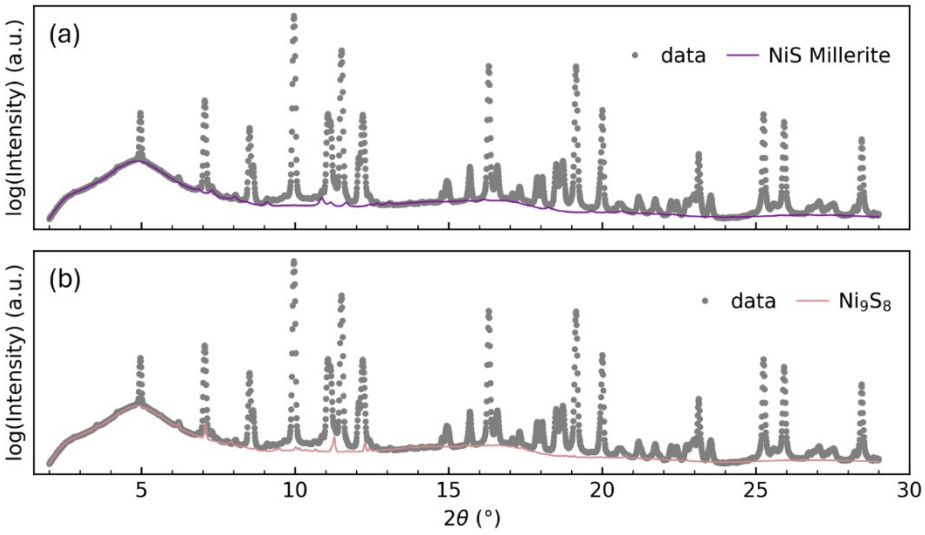

Figure S35 Diffractogram of sample 170 °C, 1 mL/min with the contributions from (a) NiS millerite and (b) Ni_9S_8.

7. Literature

1 R. B. Stubkjær, PhD Theses, Aarhus University, 2024.

2 J. Chen, X. Zhang, C. Li, X. Zhang, Y. Ren, J. He and J. Chen, *International Journal of Photoenergy*, 2020, 2020, 1–7.

3 F. Bojabady, E. Kamali-Heidari and S. Sahebian, *Mater Chem Phys*, 2023, 305, 127828.

4 S. Muneer, D. K. Sarfo, G. A. Ayoko, N. Islam and E. L. Izake, *Nanomaterials*, 2020, 10, 1756.

5 J. Ning, X. Xu, C. Liu and D. L. Fan, *J. Mater. Chem. A*, 2014, 2, 15768–15773.

6 J. J. Pérez-Bueno, R. Ramírez-Bon, Y. V. Vorobiev, F. Espinoza-Beltrán and J. González-Hernández, *Thin Solid Films*, 2000, 379, 57–63.

7 M. Arita, *Metallurgical and Materials Transactions A*, 2006, 37, 3009–3022.

8 L. Cemic and O. J. Kleppa, *Geochim Cosmochim Acta*, 1986, 50, 1633–1641.

9 M. E. Fleet, *Acta Crystallogr B*, 1972, 28, 1237–1241.

10 Stefano Merlino; Emil Makovicky, *European Journal of Mineralogy*, 2009, 21, 863–869.

11 J. D. Grice; R. B. Ferguson, *The Canadian Mineralogist*, 1974, 12, 248–252.

12 D. B. McWhan, M. Marezio, J. P. Remeika and P. D. Dernier, *Physical Review B: Solid State*, 1972, 5, 2552–2555.

13 Lundqvist D., *Arkiv for Mineralogi och Geologi*, 1947, 24, 1–12.

14 N. Elliott, *Journal of Chemical Physics*, 1960, 33, 903–905.

15 K. T. NG and D. M. Hercules, *J Phys Chem*, 1976, 80, 2094–2102.

16 N. W. Tideswell, *Corrosion*, 1972, 28, 23–25.